American Mineralogist, Volume 109, pages 1461–1477, 2024

Tourmaline chemical and boron isotopic constraints on the magmatic-hydrothermal transition and rare-metal mineralization in alkali granitic systems

Huan-Huan Wu[1,2,3,4], He Huang[1,*], Zhao-Chong Zhang[2], Shui-Yuan Yang[5], Yong-Bao Gao[3], and Adrian A. Finch[4]

[1]SinoProbe Laboratory, Institute of Geology, Chinese Academy of Geological Sciences, Beijing 100037, P.R. China
[2]State Key Laboratory of Geological Processes and Mineral Resources, China University of Geosciences, Beijing 100083, P.R. China
[3]Xi'an Center of Mineral Resources Survey, China Geological Survey, Xi'an 710100, P.R. China
[4]School of Earth & Environmental Sciences, University of St. Andrews, St Andrews, KY16 9TS, U.K.
[5]State Key Laboratory of Geological Processes and Mineral Resources, China University of Geosciences, Wuhan 430074, P.R. China

Abstract

The magmatic-hydrothermal transition in granite-related, rare-metal metallogenic systems has received great attention as economic rare metal (including rare earth) minerals reach saturation and trigger mineralization at this stage. However, deciphering the details of the melt-fluid evolution process and the distribution behavior of rare metals remains difficult. Here, we applied tourmaline chemistry and B isotopes to unravel processes at the magmatic-hydrothermal transition that are responsible for rare-metal partitioning in the Huoshibulake (HS) and Tamu (TM) REE-Nb-mineralized intrusions in Southern Tianshan, SW Central Asian Orogenic Belt. Three types of tourmaline are identified in the plutons: (1) disseminated tourmaline in the granite, with a brown-yellow core (HS-DB) and blue-green rim (HS-DG); (2) orbicular tourmaline, with a brown-yellow core (HS-OB and TM-OB) and blue-green rim (HS-OG and TM-OG); and (3) vein tourmaline (HS-V and TM-V). Compositionally, all these tourmalines exhibit extremely low Ca and Mg contents and are classified as schorl. The substitution processes of major-element variations are dominantly caused by $(Al,\square)(Fe,Na)_{-1}$ exchange vectors. Four generations of tourmaline crystallization are established based on the petrographic, compositional, and B isotopes evolution of the tourmaline. First, the HS-DB crystals crystallized from the highly evolved residual melt, and then HS-OB and TM-OB precipitated from immiscible B-rich aqueous melts during the magmatic-hydrothermal transition. Subsequently, the blue-green overgrowths (HS-DG, HS-OG, and TM-OG) crystallized from exsolved hydrothermal fluids. Finally, the formation of HS-V and TM-V resulted from another melt pulse from a deeper magma chamber. The magmatic tourmaline exhibits a narrow range of $\delta^{11}B$ values between –12.6 to –10.0‰, while the hydrothermal tourmaline shows significantly heavier and variable $\delta^{11}B$ values ranging from –10.2 to –4.9‰. The fractionation of B isotopes is reproduced by Rayleigh fractionation modeling. Lower Nb and Sn contents in the orbicular tourmaline relative to those precipitated from the residual melt, along with the lack of rare-metal minerals in the orbicules, indicate that B-rich melt/fluid exsolution does not necessarily contribute to the rare-metal mineralization. In comparison, the veins contain abundant rare-metal and REE minerals in close paragenesis with fluorite, and the vein tourmaline shows high-Nb and -Sn contents. These observations suggest that saturation of fluorite triggered the precipitation of rare metals, and fluorine played a critical role in rare metal concentration and mineralization. This study highlights the potential of tourmaline to trace the magmatic-hydrothermal transition and provide insights into rare-metal mineralization in the granitic systems.

Keywords: Multi-generation tourmaline, boron isotopes, magmatic-hydrothermal transition, rare-metal mineralization

Introduction

The magmatic-hydrothermal transition, during which the crystallization/fractionation of orthomagmatic systems evolves from melt-driven (magmatic) to fluid-driven (hydrothermal) processes, is still poorly understood because of the transient timescale and widespread overprints by post-magmatic, low-temperature alteration (Halter and Webster 2004; Michaud and Pichavant 2020). During the transition, complex melt-fluid interactions involving silicic melts, aqueous melts, and hydrothermal fluids occur (Kaeter et al. 2018; Thomas et al. 2012). Although it has been acknowledged that rare-metal granites generally originate from a fertile source with low-degree partial melting and high-degree fractional crystallization contributing significantly to rare-metal enrichment (Ballouard et al. 2020; Linnen et al. 2014; Sheard et al. 2012; Williams-Jones and Vasyukova 2023), evidence increasingly points toward the magmatic-hydrothermal transition as the critical step for hyper-enrichment and mineralization of rare metals (Ballouard et al. 2016; Carr et al. 2021;

* Corresponding author E-mail: huanghecugb@126.com. Orcid https://orcid.org/0000-0001-9055-2703

0003-004X/24/0008–1461$05.00/DOI: https://doi.org/10.2138/am-2023-9131

Zhu et al. 2015). However, clarifying the distribution behavior of rare-metal elements and their metallogenic mechanism during the transition remains challenging.

Tourmaline is a common borosilicate mineral in granitic systems that can crystallize directly from the early magmatic stage through to the late sub-solidus fluid (Liu and Jiang 2021; Yang et al. 2015). Due to its highly variable composition, stability over large *P-T* ranges, and resistance to post-crystallization alteration, tourmaline has been regarded as a reliable monitor for tracing the evolution of melt/fluid compositions (Dutrow and Henry 2011; Hong et al. 2020; Jiang et al. 2004; Slack and Trumbull 2011; van Hinsberg et al. 2011). In particular, the differential distribution of ^{11}B and ^{10}B between melts and fluids makes boron isotopes in tourmaline a potentially valuable indicator for deciphering magmatic-hydrothermal processes (Drivenes et al. 2015; Qiu et al. 2021; Zhao et al. 2021a).

The Atushi-Baicheng-Yuli alkaline rock belt, located in South Tianshan, is a transitional zone between the Central Asian Orogenic Belt and Tarim Craton, and it is composed of outcrops of alkali granite, syenite, and carbonatite, some of which host world-class rare-metal (Nb-REE) deposits [e.g., Boziguo'er Nb-REE deposit (Huang et al. 2018); the Wajilitag REE deposit (Cheng et al. 2018); the Kuoketag Nb-REE deposit (Chen et al. 2002)]. The Huoshibulake (HS) and Tamu (TM) plutons are adjacent A-type granitic plutons in the Atushi district with Nb and REE mineralization, characterized by a wide occurrence of economic minerals, e.g., most importantly columbite, synchysite, and fluocerite (Shi 2010). Tourmaline occurs in many forms in the plutons, including disseminated, orbicular, and veins, the latter two intimately associated with quartz. It records a continuous evolution from the magmatic to hydrothermal stages. Tourmaline-quartz orbicules occur widely in the two alkali granitic plutons, a texture most commonly reported in peraluminous granitic systems and considered a product of segregated B-rich melts (Drivenes et al. 2015; Harlaux et al. 2020; Hong et al. 2020; Zhao et al. 2021a). These

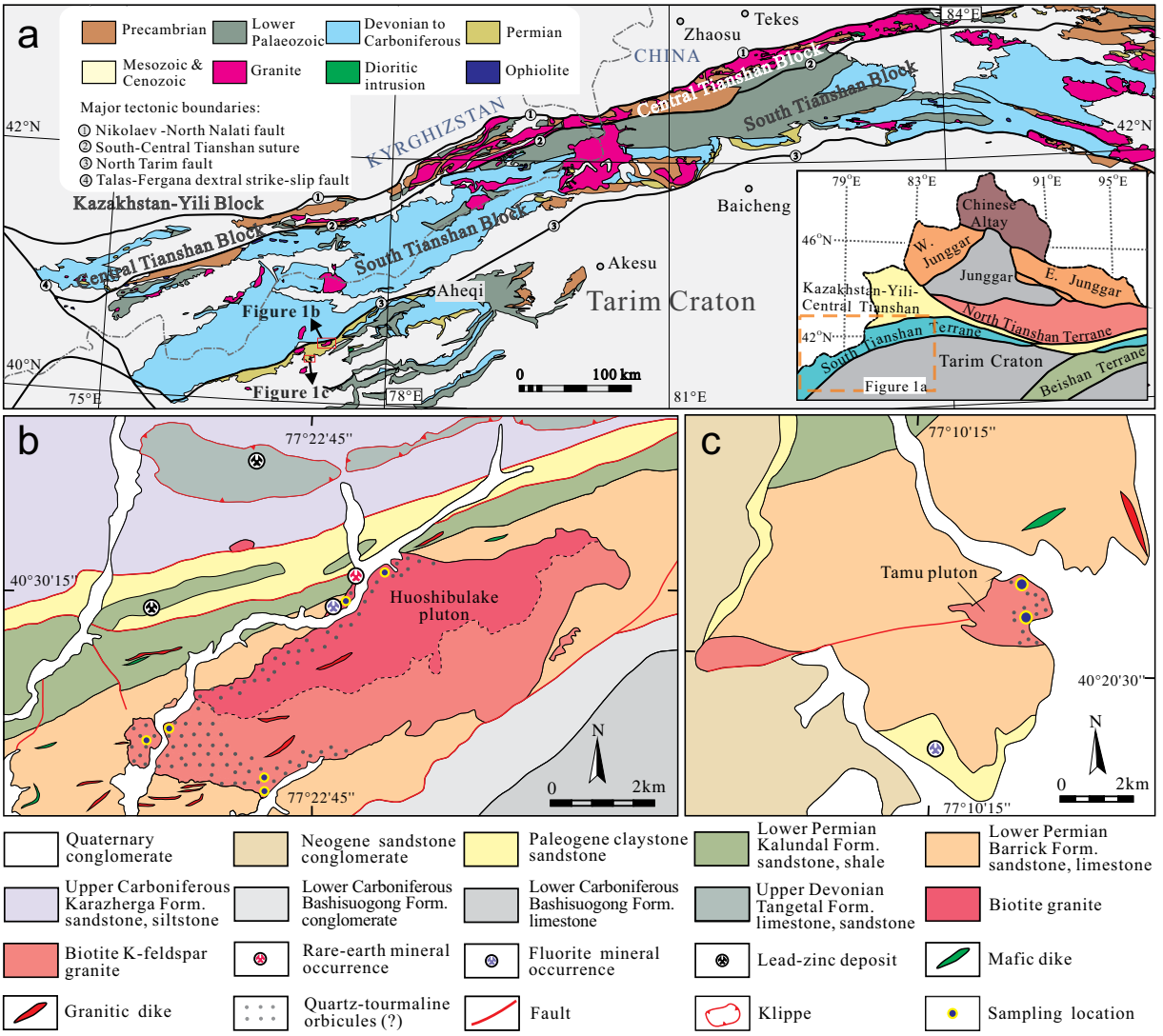

Figure 1. (**a**) Geological map of the South Tianshan Belt and the northern margin of the Tarim Craton, modified from Gao et al. (2011) and Huang et al. (2015). (**b**) Simplified geological map of the Huoshibulake pluton. (**c**) Simplified geological map of the Tamu pluton. (Color online.)

plutons show varying degrees of rare-metal mineralization in the different stages, and rare-metal minerals exhibit parageneses with specific generations of tourmaline. Consequently, the two alkali plutons offer an exceptional natural laboratory for elucidating the magmatic-hydrothermal transition and associated rare-metal mineralization within the alkali granitic systems, as seen from the perspective of tourmaline.

In this study, we carry out detailed investigations on tourmaline from the two plutons, including mineral textures, chemical compositions, and B isotopes, to reconstruct the magmatic-hydrothermal evolution. We further constrain the distribution and precipitation of Nb and REE during the magmatic-hydrothermal transition by integrating the paragenesis of economic minerals with the different types of tourmaline, as well as by evaluating variations of the ore-forming elements in the tourmaline.

Geological background

The Central Asian Orogenic Belt (CAOB) is one of the largest accretionary orogens in the world, sandwiched between the Siberian and European Cratons to the north and the Karakum-Tarim-North China Cratons to the south. The Western Xinjiang region is situated in the southwestern CAOB and can be divided into (from north to south) the Altay, Junggar Block, North Tianshan Belt (NTB), Yili–Kazakhstan Block (YKB), Central Tianshan Block (CTB), South Tianshan Belt (STB), and northern margin of the Tarim Craton (NMTC) (Fig. 1a). The STB is bounded by the Southern-Central Tianshan Suture (SCTS) to the north and by the North Tarim Suture (NTS) to the south and resulted from the Paleozoic closure of the Paleo-Asian Ocean and the subsequent collision of Tarim Block and Southwestern CAOB. During the Early Permian, the northern margin of Tarim and its adjacent areas was subjected to intracontinental extension, accompanied by regional alkaline magmatism (Wei et al. 2019; Zong et al. 2020). From Atushi in the west to Yuli in the east, this created a series of alkaline volcanic and intrusive rocks, forming a ~1100 km long alkaline-rock belt. Several rare metal deposits (e.g., Boziguo'er Nb-Ta-Zr deposit, Kuoketag Nb-Ta-Zr deposit, and Wajilitag REE deposit) and rare metal mineralized plutons (e.g., Tamu Nb-REE-mineralized pluton, Huoshibulake REE-mineralized pluton, and Bashisuogong Nb-REE complex) have been found in the belt (Nechaev et al. 2021; Xie et al. 2022), revealing significant rare-metal metallogenic potential in the area.

The Huoshibulake and Tamu plutons are situated in the northeast of Atushi city (Fig. 1a). The Huoshibulake pluton has an outcrop of 30 km^2 and consists of two transitional units from the center outward: biotite granite and biotite K-feldspar granite (Figs. 1b and 2a). The Tamu pluton, located ~10 km southwest of the Huoshibulake pluton (Fig. 1c), shows similar petrographic features to the Huoshibulake pluton. The major minerals in both plutons are alkali feldspar, quartz, biotite, and minor alkali amphibole, fluorite, and tourmaline. Major economic rare metal (including REE) minerals consist of monazite, columbite, synchysite, and fluocerite. Both plutons exhibit high SiO_2 (74.6–78.1 wt%), Al_2O_3 (11.5–12.6 wt%), and total alkali (7.85–8.96 wt%) concentrations, while having extremely low CaO (0.10–1.22 wt%) and MgO (0.02–0.22 wt%) concentrations (Huang et al. 2012). Multi-mineral U-Pb dating of both plutons yielded an identical age of ~273 Ma, revealing the early Permian emplacement (Wu et al. 2024).

Tourmaline occurrence and sample descriptions

Tourmaline is widespread and shows similar features in both the Huoshibulake and Tamu plutons. Based on the textural characteristics, three distinct types of tourmaline are identified: (1) disseminated subhedral to anhedral tourmaline in granite matrix; (2) tourmaline in tourmaline-quartz orbicules (termed "orbicular tourmaline" in this paper); and (3) tourmaline in tourmaline-quartz veins. The characteristics of these tourmalines are described as follows:

Disseminated tourmaline in the Huoshibulake pluton

Disseminated tourmaline is found in most granite samples from the Huoshibulake pluton (Figs. 2b–2c), but is absent in the Tamu pluton. Tourmaline grains of this type are distributed within the granitic matrix as isolated subhedral to anhedral grains (Figs. 2d–2e) or grain aggregates (Fig. 2f), tens to hundreds of micrometers long, commonly coexisting with quartz, biotite, and K-feldspar grains. They generally contain yellow-brown (abbreviated as HS-DB, where "HS", "D", and "B" represent pluton name, texture, and color of tourmaline; similar rules apply to the abbreviations used below) mantles with occasional blue-green rims (HS-DG), which are also distinguished from each other by different degrees of backscattered brightness in the backscattered electron images (BSE) (Figs. 2g–2i). A notable phenomenon is a large abundance of rare-metal minerals (e.g., zircon, monazite, columbite, synchysite, fluocerite) enclosed in these disseminated tourmalines (Figs. 2g–2i and 3a–3c). These rare-metal minerals are highly concentrated in close proximity to fluorite (Figs. 3a–3c).

Tourmaline in tourmaline-quartz orbicules

Tourmaline-quartz orbicules have a widespread occurrence in both Huoshibulake and Tamu plutons (Figs. 1b–1c). The orbicules are randomly distributed and commonly several to more than 10 cm in diameter (Figs. 4a–4b). A typical orbicule consists of a tourmaline core, a tourmaline-quartz mantle, and a leucocratic rim (Fig. 4b). The core consists mainly of clusters of euhedral tourmaline with minor quartz grains, whereas tourmaline (~50 vol%) is intergrown with quartz (~40 vol%) in the mantle, along with minor relicts of partially replaced perthitic K-feldspar (~10 vol%). Minor biotite, muscovite, and fluorite are also present in the orbicules, but rare-metal minerals are lacking. A 0.5–1 cm wide leucocratic rim can be recognized surrounding the orbicules. The fine-grained, granitic-textured rim is compositionally the same as the surrounding granite, but with lower proportions of mafic minerals. The tourmaline in orbicules shows a sieve-like texture characterized by the intergrowth of tourmaline and quartz (Figs. 4c–4d). Two types of tourmaline are distinguishable in plane-polarized light: tourmaline at the core of the crystals shows yellow to brown pleochroism (HS-OB and TM-OB), and tourmaline at the rim exhibits green to blue pleochroism (HS-OG and TM-OB) (Figs. 4c–4d). When viewed using BSE imaging, the green rims consistently show lower brightness than the brown cores (Figs. 4e–4f).

Tourmaline in tourmaline-quartz vein

Tourmaline-quartz veins are well developed in the Huoshibulake and Tamu plutons, with variable widths ranging from several to tens of centimeters and lengths from several to tens of meters

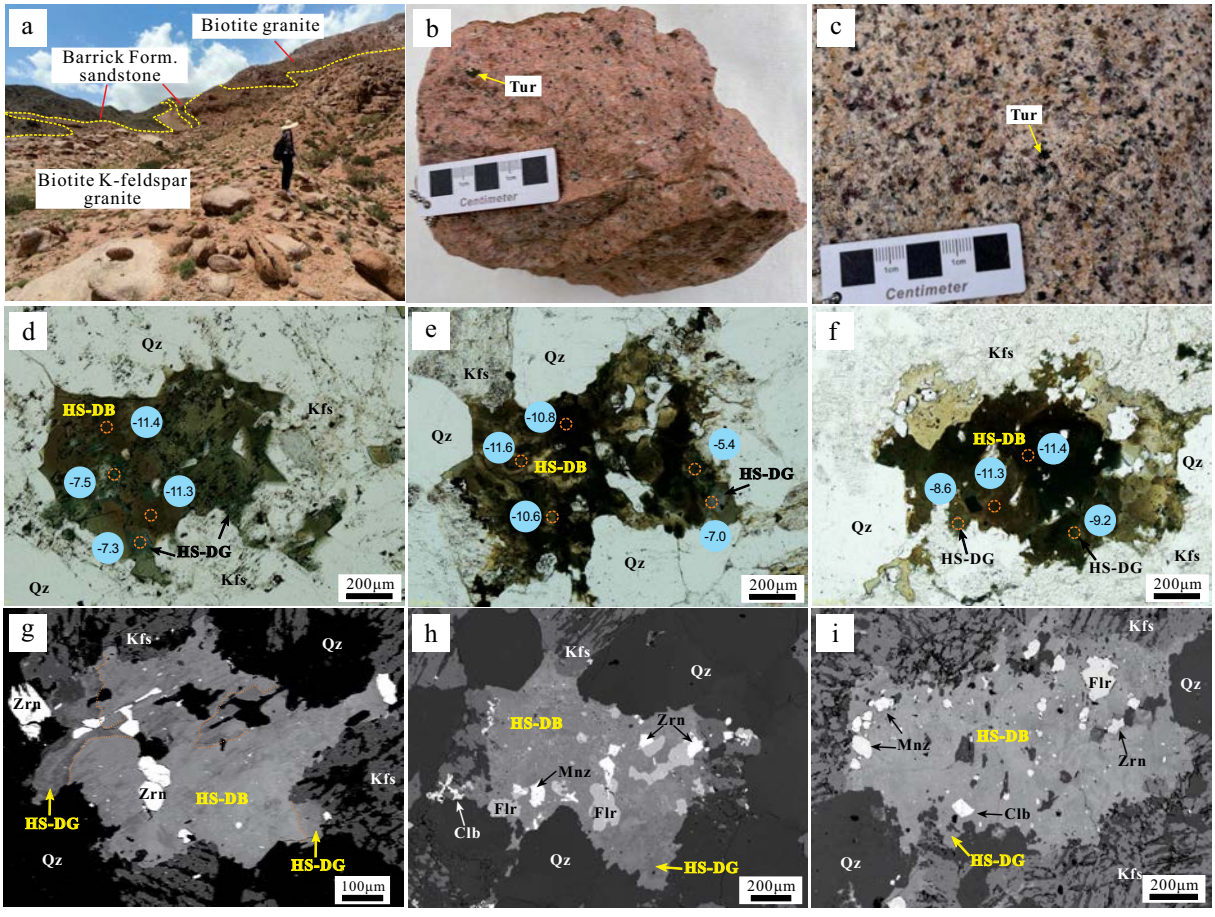

Figure 2. (**a**) Field photo showing the contact relationship between the Huoshibulake pluton and the surrounding rock. (**b** and **c**) Photographs of hand specimens of disseminated tourmaline, showing dispersed tourmaline crystals in the Huoshibulake K-feldspar biotite granite and biotite granite, respectively. (**d** and **e**) Plane-polarized light photomicrographs of sub- to euhedral tourmaline, with brown-yellow pleochroism at the core and blue-green pleochroism at the rim. (**f**) Plane-polarized light photomicrograph of anhedral tourmaline aggregate. (**g**–**i**) BSE images of disseminated tourmaline. Orange circles and blue circles with numbers show the analyzed location and $\delta^{11}B$ values for boron isotopic analysis, respectively. Tur = tourmaline; Qz = quartz; Kfs = K-feldspar; Pl = plagioclase; Flr = fluorite; Mnz = monazite; Zrn = zircon; Clb = columbite. (Color online.)

(Figs. 5a–5b). Most veins exhibit near-vertical orientation and are generally parallel in the same outcrop (Fig. 5a). These veins are composed mainly of tourmaline and quartz, with minor muscovite and fluorite (Fig. 5c). The tourmaline from these veins (HS-V and TM-V) exhibits yellow to blue pleochroism; most grains show distinct growth zonation (Figs. 5d–5f), which is also recognizable in the BSE images (Figs. 5g–5i). A large number of rare-earth minerals (e.g., synchysite, fluocerite, and monazite) and columbite are observed in these veins (Figs. 3d–3f) in contrast to the orbicules. Most rare-metal minerals are precipitated as inclusions in, or near, fluorite (Figs. 3e–3f).

Analytical methods

Electron probe microanalysis (EPMA)

The major and minor elements of tourmaline were analyzed with a JEOL JXA-8230 Electron Probe Microanalyzer equipped with five wavelength-dispersive spectrometers (WDS) at the Laboratory of Microscopy and Microanalysis, Wuhan Microbeam Analysis Technology Co., Ltd. The samples were coated with a thin conductive carbon film before analysis. The precautions suggested by Zhang and Yang (2016) were used to minimize the difference in carbon film thickness between samples and obtain a ca. 20 nm approximately uniform coating. Operating conditions for quantitative WDS analyses involved an accelerating voltage of 15 kV, a beam current of 20 nA, and a 10 μm spot size. Data were corrected online using a ZAF (atomic number, absorption, fluorescence) correction procedure. The content of B was calculated based on the mole ratio of B:Si = 1:2, and then involved in the ZAF correction procedure. The peak counting time was 10 s for Ca, Mg, K, F, Si, Al, Ti, Na, and Cl, and 20 s for Fe and Mn. The background counting time was 1/2 of the peak counting time on the high- and low-energy background positions. The following standards were used: diopside (Ca, Mg), microcline (K), barium fluoride (F), olivine (Si), pyrope garnet (Fe, Al), jadeite (Na), halite (Cl), rutile (Ti), rhodonite (Mn).

LA-ICP-MS and LA-MC-ICP-MS analysis

In situ trace-element analyses of tourmaline were conducted at the State Key Laboratory of Geological Processes and Mineral Resources (GPMR) in China University of Geosciences (Wuhan), using a RESOlution S-155 laser ablation system coupled to a Thermo iCAP-Q_c inductively coupled plasma-mass spectrometer (LA-ICP-MS). The U.S. Geological Survey (USGS) reference glasses (BIR-1G, BCR-2G, and BHVO-2G) and the NIST SRM 612 and 610 glasses were analyzed after every eight tourmaline sample spots. The ablation protocol employed a spot diameter of 33 μm at a 10 Hz repetition rate for 40

s. The approximate depth of ablation was 30–50 µm. Helium was used as the carrier gas to the ICP-MS. The isotope ^{29}Si was used as the internal standard in conjunction with the Si concentrations determined by EPMA. External calibration was performed using the USGS reference glasses. The NIST glasses were used for correcting the signal drift. Raw data reduction was performed offline using the ICPMSDataCal software (Liu et al. 2010), and to reduce the effect of the signal variability with depth on the test results, the same integration interval of the signal was chosen for the sample and standard.

Most of the in situ B isotopic compositions of tourmaline were measured at the GPMR using the same laser ablation system coupled to a Nu Plasma II multicollector ICP-MS. Additional analyses were conducted at the National Research Center for Geoanalysis, Chinese Academy of Geological Science (CAGS), using a Neptune Plus fs-LA-MC-ICP-MS (Thermon Fisher Scientific, Germany) in combination with a 343 nm femtosecond laser ablation system (J-100, Applied Spectra, West Sacramento, California, U.S.A.). Both analyses were carried out with a beam diameter of 50 µm and a 10 Hz repetition rate. The ^{11}B and ^{10}B were collected statically and simultaneously with two Faraday cups. The instrumental mass fractionation (IMF) was calibrated using the sample standard bracketing (SSB) method. The international tourmaline standard IAEA B4 ($\delta^{11}B$ = –8.71‰; Tonarini et al. 2003a) was adopted as the external standard during the two analyses. The similarity of IMF values (Online Materials[1] Table OM1) determined for the chemically distinct tourmaline standards, including two in-lab tourmaline reference materials used at the GPMR [schorl HS#112566 and dravite HS#108796 from the Harvard Mineralogical Museum (Dyar et al. 2001)], and one used at the CAGS [IMR RB1 (Hou et al. 2010)], all demonstrate insignificant matrix effects. The analytical precision is estimated to be better than 0.5‰ (±2σ) based on the replicated analyses of reference tourmaline during this study. More detailed descriptions of the two analytical methods can be found in Zhao et al. (2021a) and Long et al. (2021), respectively. Ten replicated spots were measured to monitor the analytical errors between the two labs, and the results showed near identical $\delta^{11}B$ values between the two analyses (all <0.2‰, see details in Online Materials[1] Table OM1).

Results

Major element compositions

A total of 264 spots among 37 tourmaline grains were analyzed by EPMA, and the results are given in Online Materials[1] Table OM2. Structural formulas were calculated based on the general formula of $XY_3Z_6T_6O_{18}(BO_3)_3V_3W$, where X = Ca^{2+}, Na^{+}, K^{+}, X_{vac} (vacancy); Y = Mg^{2+}, Fe^{2+}, Mn^{2+}, Al^{3+}, Ti^{4+}, Fe^{3+}; Z = Mg^{2+}, Al^{3+}, Fe^{3+}; T = Si^{4+}, Al^{3+}, (B^{3+}); V = OH^{-}, O^{2-}; and W = OH^{-}, F^{-}, O^{2-} (Henry et al. 2011). Tetrahedral and octahedral sites (T+Z+Y) were normalized to 15 cations apfu (atoms per formula unit).

Overall, comparable to those of tourmalines crystallized from peraluminous granitic systems (e.g., Zhao et al. 2019, 2022), all tourmaline samples from the Huoshibulake and Tamu plutons show relatively high SiO_2 (32.50–36.03 wt%), Al_2O_3 (21.77–33.21 wt%), FeO^T (13.98–24.64 wt%) contents, and low TiO_2 (0.00–2.95 wt%), MnO (0.00–0.15 wt%), MgO (0.00–1.19 wt%), CaO (0.00–1.69 wt%), Na_2O (1.69–2.57 wt%), K_2O (0.008–0.18 wt%), F (0.00–1.24 wt%), and Cl (<0.07 wt%) contents. Notably, most tourmaline shows extremely low CaO contents (mostly <0.1 wt%), except for the HS-DB ones that exhibit much higher contents (0.003–1.69 wt%). According to the X-site occupancy-based classification of Henry et al. (2011), all tourmalines are members of the alkali series (Fig. 6a). In the Al-Fe-Mg ternary diagrams of Henry and Guidotti (1985), the tourmaline samples studied exhibit a narrow variation and plots in the field of Li-poor granite (Fig. 6b).

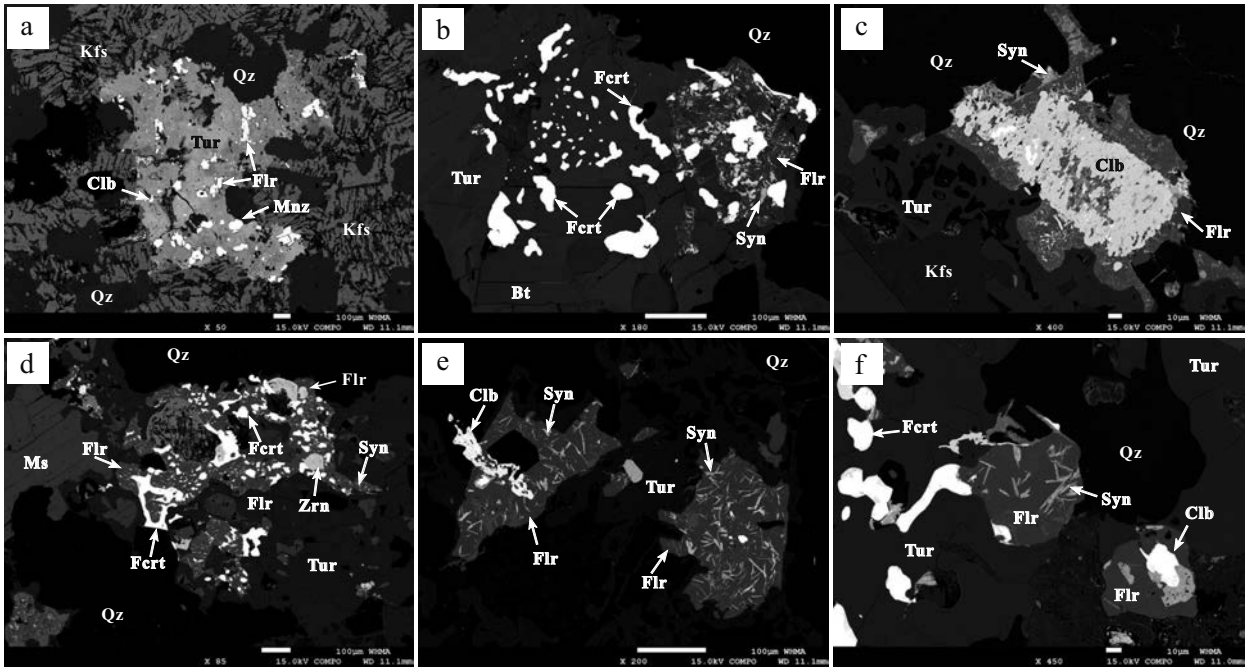

Figure 3. BSE images of disseminated tourmaline from the Huoshibulake pluton (**a**–**c**) and vein tourmaline from the Huoshibulake (**d**) and the Tamu (**e** and **f**) plutons showing the close paragenesis between fluorite and rare-metal minerals. (**a**) Typical disseminated tourmaline with abundant inclusions of columbite, fluorite, and monazite; (**b**) a strongly mineralized area with abundant fluocerite and synchysite showing paragenesis with fluorite; (**c**) anhedral columbite and abundant acicular synchysite included in a fluorite grain; (**d**) a large amount of rare-earth minerals (synchysite, fluocerite, and monazite) and columbite deposited in a F-rich domain; (**e** and **f**) columbite and acicular synchysite crystallized in fluorite droplets. Tur = tourmaline; Qz = quartz; Kfs = K-feldspar; Ms = muscovite; Flr = fluorite; Mnz = monazite; Clb = columbite; Fcrt = fluocerite; Zrn = zircon; Syn = synchysite.

Moreover, all tourmaline is Fe-rich and Mg-poor, with restricted Mg/(Mg+Fe) (0.00 to 0.09) and Na/(Na+Ca) (0.64 to 1.00) ratios, plotting in the field of the schorl series on the ^{X}[□/(□+Na)] vs. Mg/(Mg+Fe) and ^{X}[Na/(Na+Ca)] vs. Mg/(Mg+Fe) diagrams (Figs. 7a–7b). The blue-green tourmaline (i.e., HS-DG, HS-OG, and TM-OG types) at the rim exhibits significantly lower Fe and Ti contents but higher Al and X-site vacancy contents compared to the yellowish-brown tourmaline (HS-DB, HS-OB, and TM-OB types) in the core (Figs. 8a–8d). The yellowish-brown tourmaline has higher Ti contents than those in blue-green ones, consistent with the suggestion by Trumbull et al. (2007) that Ti content in tourmaline is the primary control for pleochroism. Most tourmaline crystals from HS-DB, HS-OB, HS-V, TM-OB, and TM-V types have >3 apfu Fe and <6 apfu total Al, while ones from HS-DG, HS-OG, and TM-OG mainly possess <3 apfu Fe and >6 apfu total Al (Figs. 7d and 8a–8b).

Trace-element compositions

The trace elements of 187 spots among 29 tourmaline grains were analyzed by LA-ICP-MS, all of which followed EPMA to ensure spot locations. The results are listed in Online Materials[1] Table OM2. The median concentrations of most trace elements range from 0.1 to 10 ppm, while Li, Zn, Ga, and Sn have the highest median concentrations, up to hundreds of ppm, and Sc, Sr, and Ce show median contents of tens of ppm. Concentrations of some trace elements show large variations over several orders of magnitude, such as Li (12.8–256 ppm), Zn (70.3–592 ppm), Sr (0.29–602 ppm), Nb (0.12–71.7 ppm), Sn (4.66–2542 ppm), and REE (0.25–170 ppm). In the Huoshibulake pluton, earlier tourmaline (HS-DB and HS-OB) exhibits higher Sc, Ga, Sr, Sn, and Nb and lower Li concentrations than later tourmaline (HS-DG and HS-OG, Figs. 8e–8j). However, the latest-stage tourmaline in veins (HS-V) shows an inverse trend with high-Sc, -Ga, -Sr, -Sn, and -Nb abundances. Similar variations are also observed in tourmaline from the Tamu pluton (i.e., TM-OG has higher Li and lower Sc, Ga, Sr, Sn, and Nb contents than those of TM-OB and TM-V). All tourmaline spots display large total REE abundance variations (Fig. 8k). Variation diagrams of representative element pairs show significant positive correlations between Hf vs. Zr, Ta vs. Nb, Sr vs. Sn, and Ce vs. La (Fig. 9).

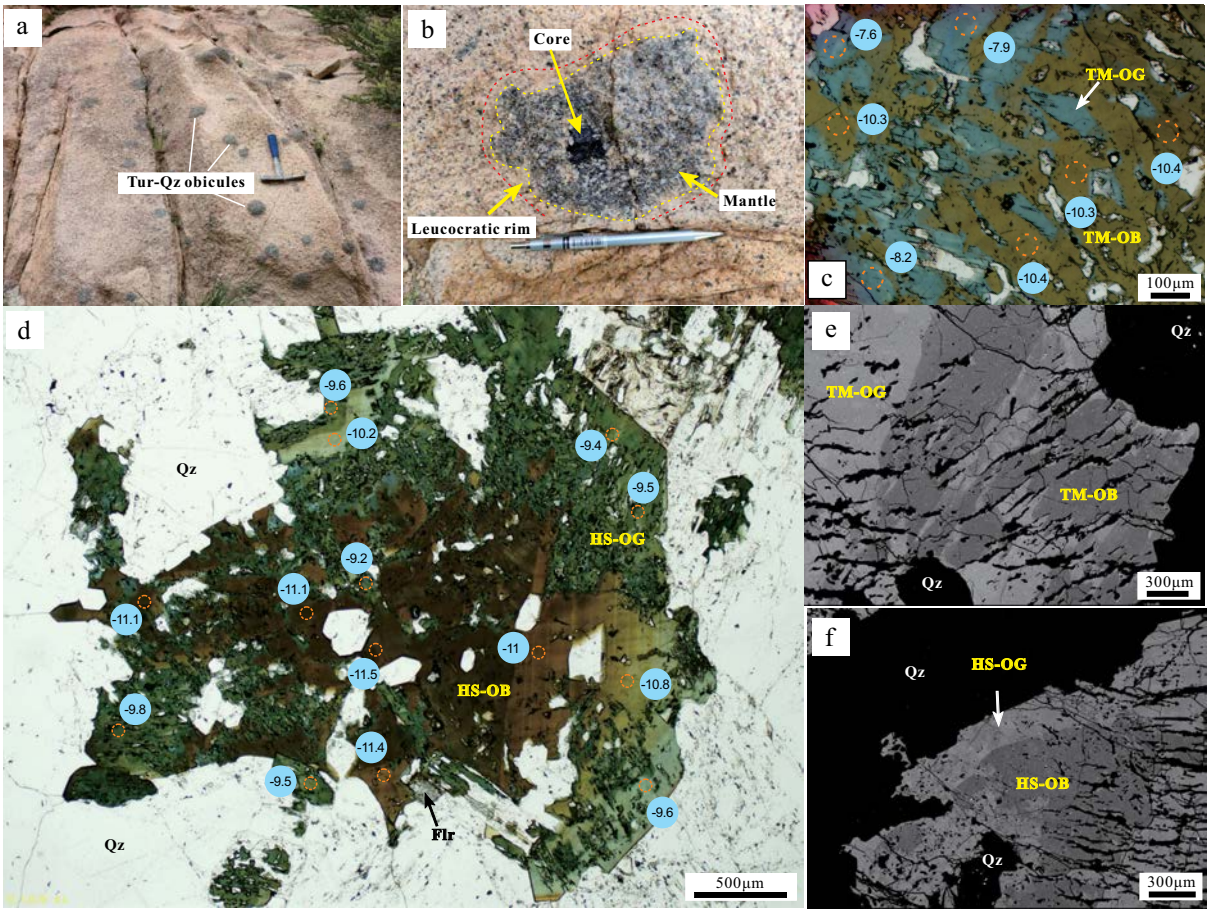

Figure 4. (**a** and **b**) Photographs of outcrops of tourmaline-quartz orbicules from the Huoshibulake and Tamu plutons, showing typical core-mantle-rim texture. (**c** and **d**) Plane-polarized light photomicrograph of sieve-like tourmaline intergrown with quartz, showing the yellow-brown core and blue-green rim. (**e** and **f**) BSE images of orbicular tourmaline with dark cores and light rims. Orange circles and blue circles with numbers show the analyzed location and δ^{11}B values for boron isotope, respectively. Tur = tourmaline; Qz = quartz; Flr = fluorite; Mnz = monazite. (Color online.)

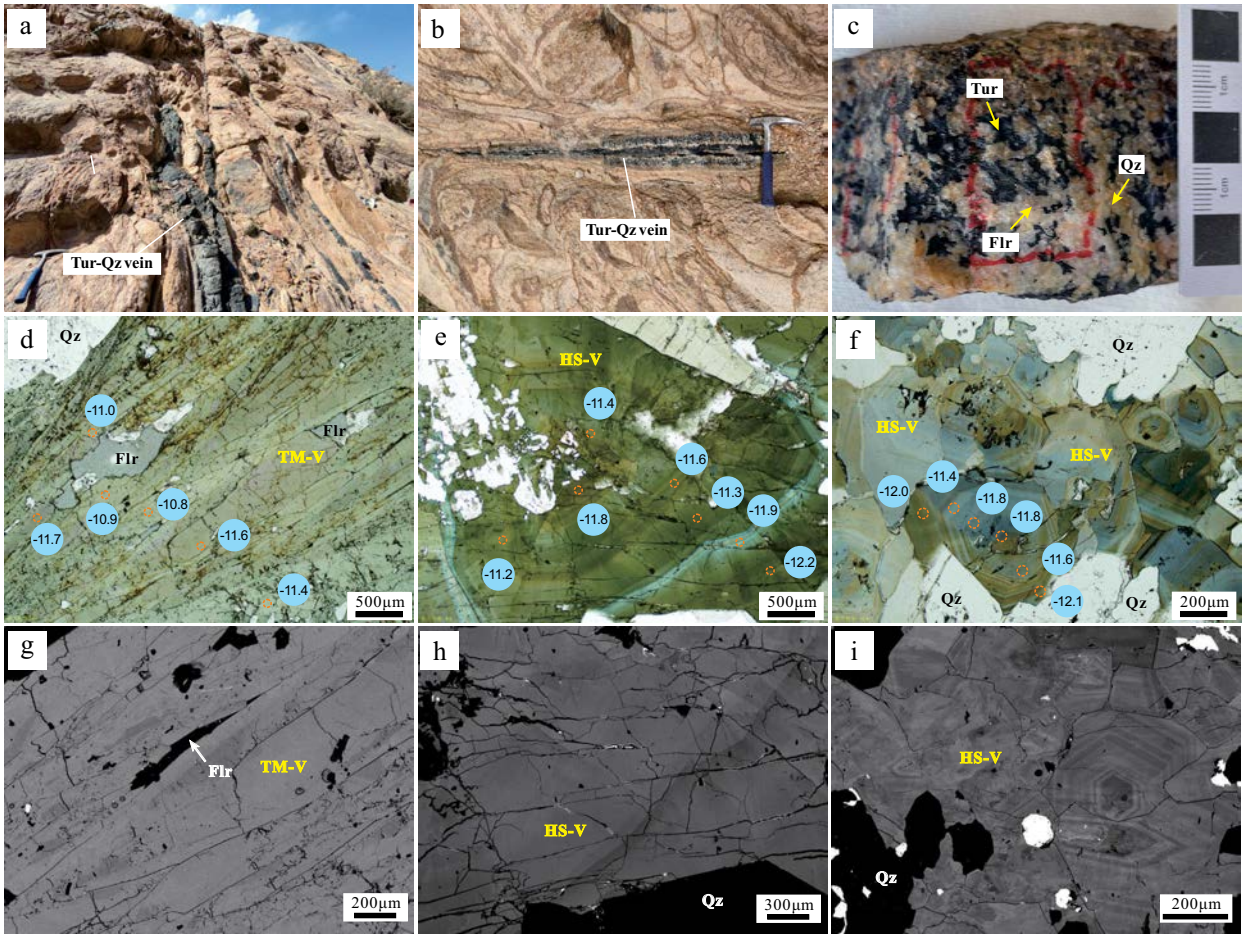

Figure 5. Photographs showing texture, mineralogy, and B isotopic characteristics of tourmaline-quartz veins in the Huoshibulake and Tamu plutons. (**a** and **b**) Near-parallel tourmaline-quartz veins outcrops; (**c**) hand specimen photo showing the sub- to euhedral tourmaline intergrowth with quartz and fluorite; (**d**–**f**) plane-polarized light photomicrograph of tourmaline grains with growth zonation and near identical B isotopic compositions. Tourmaline grains (**d**) are sectioned oblique to the c axis, and (**e** and **f**) parallel to the c axis. Orange circles and blue circles with numbers show the analyzed location and $\delta^{11}B$ values for boron isotope, respectively. (**g**–**i**) Representative BSE images showing the concentric zoning in tourmaline hosted in the veins. Tur = tourmaline; Qz = quartz; Flr = fluorite. (Color online.)

Boron isotopic composition

A total of 228 B isotopic compositions (including 10 replicated spots for checking consistency) among 29 tourmaline grains were determined by LA-ICP-MS, and the results are listed in Online Materials[1] Table OM1 and plotted in Figure 10. The $\delta^{11}B$ of five types of tourmaline from the Huoshibulake pluton range from –12.6 to –5.2‰, falling in the range of typical granitic magmas (–20 to –5‰, Trumbull and Slack 2018). Tourmaline spots from the HS-OB, HS-DB, and HS-V types exhibit restricted ranges of $\delta^{11}B$ from –11.8 to –10.2‰ (mean = –10.9‰, n = 26), –12.6 to –10.0‰ (mean = –11.1‰, n = 30), and –11.7 to –10.1‰ (mean = –10.9‰, n = 23), respectively. In comparison, blue-green tourmaline from HS-OG and HS-DG groups shows significantly higher values of $\delta^{11}B$ ranging from –9.8 to –7.4‰ (mean = –8.7‰, n = 32) and –10.2 to –5.2‰ (mean = –8.2‰, n = 29). The $\delta^{11}B$ values of three types of tourmaline from the Tamu pluton range from –12.6 to –4.9‰. Similar to the isotopic fractionation observed in the Huoshibulake pluton, tourmaline grains of TM-OB and TM-V types show relatively lower $\delta^{11}B$ values ranging from –12.6 to –10.0‰ (mean = –11.2‰, n = 34) and –12.2 to –10.3‰ (mean = –11.3‰, n = 26), while the blue-green tourmaline grains from TM-OG type have higher values ranging from –9.7 to –4.9‰ (mean = –6.8‰, n = 28).

Discussion

Formation of tourmaline

The Huoshibulake and Tamu plutons are two adjacent A-type rare-metal granites in the South Tianshan alkaline rock belt. Multi-mineral geochronological studies have shown that both were emplaced at ~273 Ma (Zhang et al. 2010; Wu et al. 2024). They are both characterized by high SiO_2, Al_2O_3, and alkali contents, low FeO^T, MgO, and CaO contents, and enrichment of large ion lithophile elements (e.g., Rb) and high field strength elements (e.g., Nb, Ta, Zr, Hf) (Zhang and Zou 2013; Zong et al. 2020). Their similar whole-rock Nd isotopes and zircon Hf-O isotopes are consistent with them being genetically related (Wei

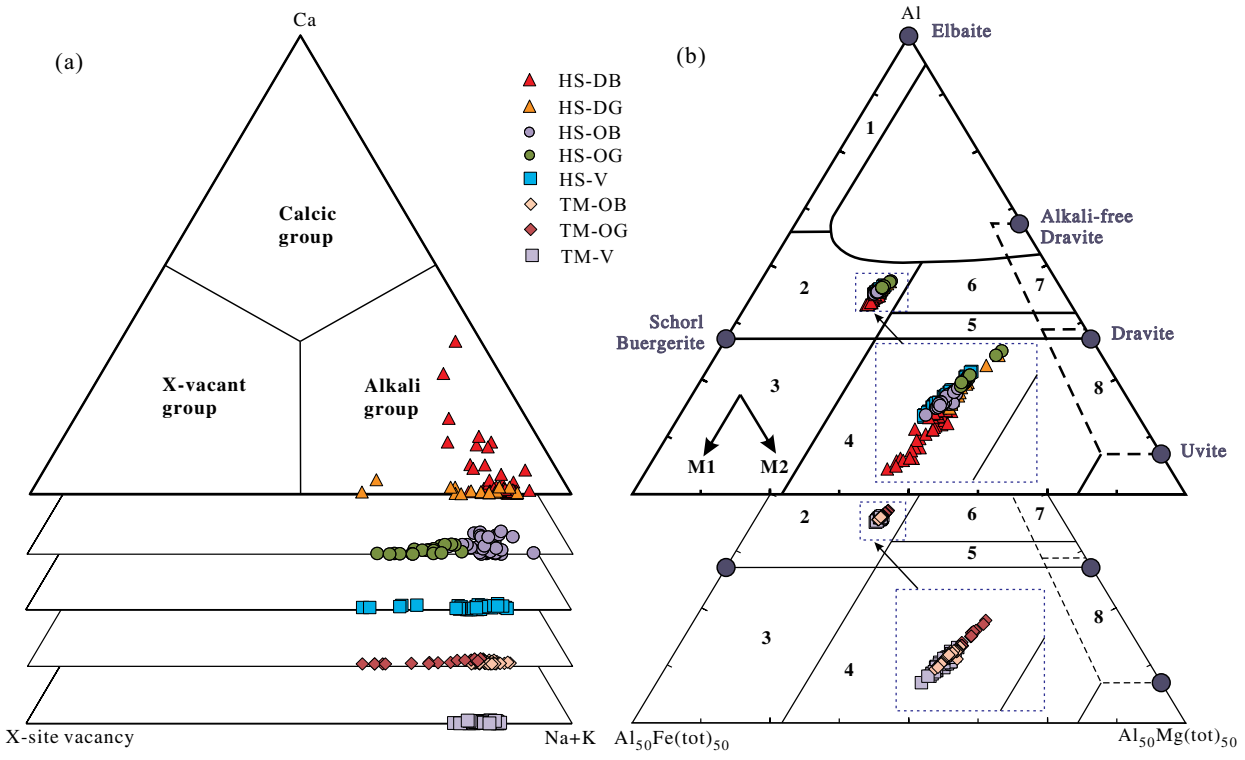

Figure 6. (**a**) Classification diagrams based on X-site occupancy (modified after Henry et al. 2011) and (**b**) Al-Fe-Mg ternary diagrams (modified after Henry and Guidotti 1985) of tourmaline from the Huoshibulake and Tamu plutons showing compositional variations of tourmaline from various source rocks. 1 = Li-rich granitoid pegmatites and aplites; 2 = Li-poor granitoids and their associated pegmatites and aplites; 3 = Fe^{3+}-rich quartz-tourmaline rocks (hydrothermally altered granites); 4 = metapelites and metapsammites coexisting with an Al-saturating phase; 5 = metapelites and metapsammites not coexisting with an Al-saturating phase; 6 = Fe^{3+}-rich quartz-tourmaline rocks, calc-silicate rocks, and metapelites; 7 = low-Ca metaultramafics and Cr,V-rich sediments; 8 = metacarbonates and metapyroxenites. M1 = $Fe^{3+}Al_{-1}$ and $(Fe^{2+},OH^{-})(Al,O^{2-})_{-1}$; M2 = $(Mg,OH^{-})(Al,O^{2-})_{-1}$; HS = Huoshibulake pluton; TM = Tamu pluton; DB = yellow-brown core of disseminated tourmaline; DG = blue-green rim of disseminated tourmaline; OB = yellow-brown core of orbicular tourmaline; OG = blue-green rim of orbicular tourmaline; V = vein tourmaline. (Color online.)

et al. 2019; Zhang and Zou 2013). Combined with their indistinguishable petrographic features, Huang et al. (2012) concluded that they are twin plutons derived from a single deeper magma chamber in a multi-level plumbing system, which ultimately originated from partial melting of the mafic lower crust.

A distinct characteristic of the Huoshibulake and Tamu plutons is the widespread, multi-generation crystallization of tourmaline. Consistent with the whole-rock composition, all types of tourmaline in the two plutons show extremely low CaO (0–1.68 wt%) and MgO (0–1.19 wt%) contents, indicating their crystallization from highly evolved magmatic-hydrothermal systems (Zheng et al. 2022). In the Mg-Fe plot, tourmalines from the two plutons do not show any observable substitution trend of $MgFe_{-1}$ because of low Mg contents, but reveal a substitution trend consistent with the $FeAl_{-1}$ (Fig. 7c). The higher Fe and lower total Al contents in tourmaline crystals from the yellowish-brown tourmaline (HS-DB, HS-OB, and TM-OB types) than those of blue-green tourmaline (HS-DG, HS-OG, and TM-OG types) suggests that Fe could be incorporated into the Z-site to substitute for Al (up to 1.11 apfu in this study) when Al is deficient. Conversely, Al can be incorporated into the Y-site to substitute Fe (up to 0.77 apfu in this study) when Al became elevated to excess in the Z-site during magmatic evolution. Charge balance is maintained by the adjustment of the vacant X-site or substitution between O and OH (Fig. 7e). The HS-DB tourmaline in the Huoshibulake pluton is disseminated interstitially between quartz and K-feldspar, brown in color without fine-scale zonation (Figs. 2d–2f), and in some cases, the rim of HS-DB tourmaline is replaced by K-feldspar with a few small irregular tourmaline residues (Fig. 2e), consistent with the characteristics of magmatic tourmaline in other highly evolved granites (Zhao et al. 2019, 2021a; Yang et al. 2015). The Mg/(Mg+Fe) ratio generally decreases with magmatic differentiation (Yang et al. 2015); higher Mg/(Mg+Fe) ratios of the HS-DB tourmaline compared to other tourmaline types (Figs. 7a–7b) are consistent with earlier crystallization of the HS-DB tourmaline. This is also supported by the linear relationships shown in the plots of Al^{tot} vs. Fe^{tot} and Al^{tot} vs. X-site vacancy that the compositional evolution of most tourmaline types in the Huoshibulake and Tamu plutons were mainly controlled by the exchange of $(Al,\square)(Fe,Na)_{-1}$ while the HS-DB show an exchange trend of $(Al,Na)(Ca,Mg)_{-1}$ (Figs. 7d–7f). Thus, we conclude that the HS-DB tourmaline is of primary magmatic origin.

Tourmaline-quartz orbicules have been widely reported in evolved peraluminous granitic rocks with different tectonic settings and ages worldwide (Yang et al. 2015; Trumbull et

al. 2007). However, they have rarely been reported in alkali granitic systems. Although a hydrothermal origin related to post-magmatic alteration has been proposed in some studies (e.g., Rozendaal and Bruwer 1995), the orbicules are more commonly interpreted as crystallization products of late-magmatic, volatile-rich melts in which volatile-rich phases are incapable of escaping from the magmatic system (Balen and Broska 2011; Trumbull et al. 2007; Yang et al. 2015). The tourmaline-quartz orbicules in the Huoshibulake and Tamu plutons are isolated in the granites without fracture networks or veinlets (denoting fluid pathways)

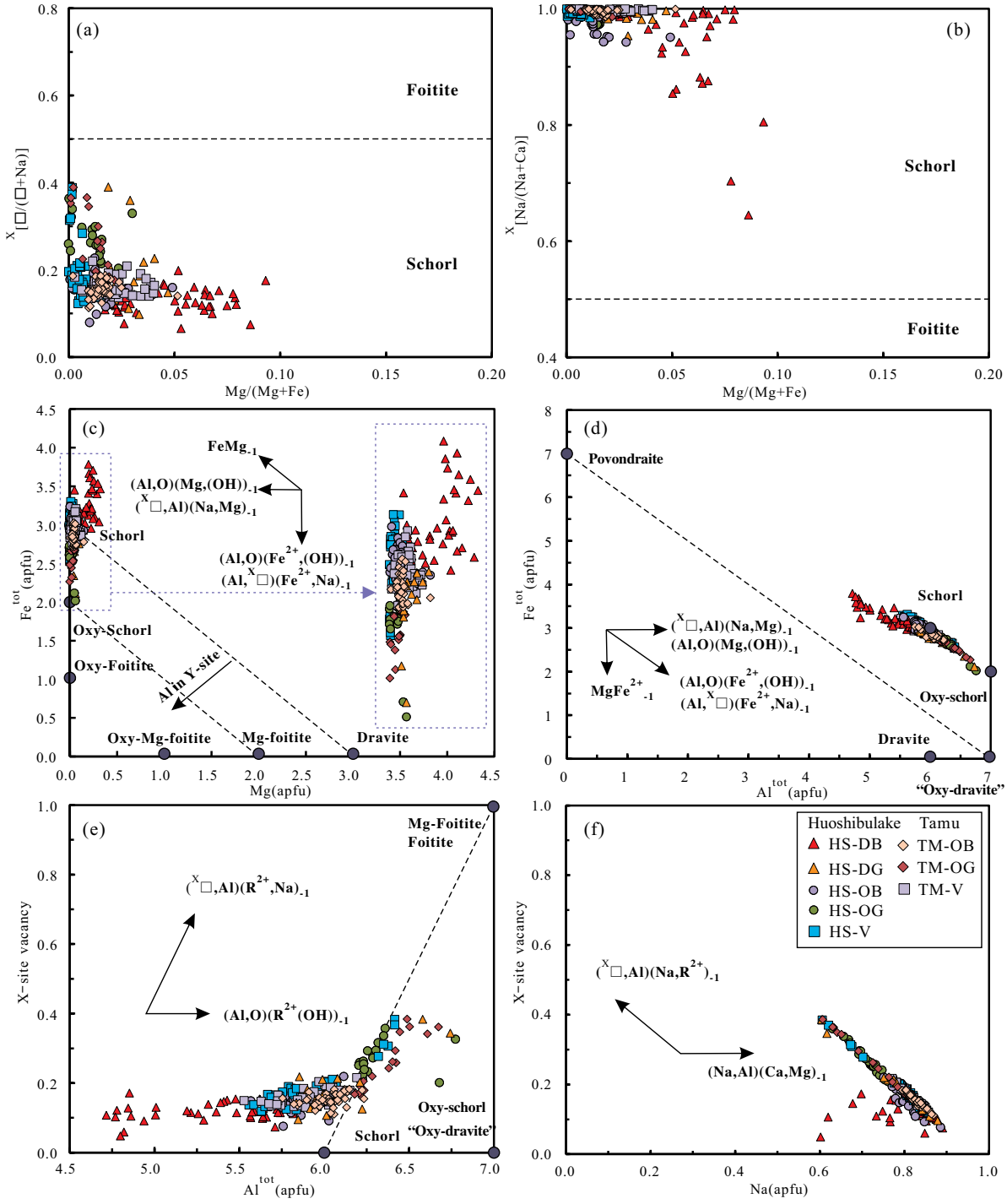

Figure 7. (**a** and **b**) Classification of tourmaline from the Huoshibulake and Tamu plutons (modified after Trumbull and Chaussidon 1999; Henry and Dutrow 2012); (**c**–**f**) chemical discrimination diagrams for tourmaline from the Huoshibulake and Tamu plutons, showing their compositional evolution trends and exchange vectors (modified after Henry and Dutrow 1990, 2012). Abbreviations are same as Figure 6. (Color online.)

connecting them to the surrounding rock (Figs. 4a–4b). Besides, the orbicular tourmaline exhibits extremely low Mg and low Ca contents, inconsistent with the origination of external fluids that are generally rich in Mg and Ca (Slack 1996; Trumbull et al. 2007). Some trace-element pairs [e.g., Nb-Ta (Ballouard et al. 2016); Zr-Hf (Zaraisky et al. 2009)] show similar enrichment behaviors during magmatic-hydrothermal evolution. The positive correlations of these element pairs shown in Figure 9 are consistent with a continuous magmatic-hydrothermal evolution trend. It has been proposed that an aqueous melt phase, rich in fluxing elements (e.g., P, Li, B, and F), can separate from the residual melt at the final stage of highly evolved granitic systems (Balen and Broska 2011; Thomas et al. 2005; Veksler et al. 2002). Evidence from both experiments and melt inclusions in natural samples reveals that B has a higher affinity for partitioning into such an aqueous melt compared with normal aluminosilicate melt and aqueous fluid (Thomas et al. 2003; Veksler et al. 2002). In our case, the similar pleochroism and B isotopic compositions of the HS-OB and HS-DB tourmalines allow their crystallization from compositionally and isotopically similar melts. For these reasons, the tourmaline orbicules are interpreted to form from immiscible B-rich aqueous melts during the magmatic-hydrothermal transition. The lower Mg/(Mg+Fe) ratios of the HS-OB tourmaline relative to the HS-DB ones can be attributed to the precipitation of biotite before the exsolution of the immiscible B-rich melts, analogous to the scenario of Qitianling granite in South China (Yang et al. 2015). Feldspar is the major Sr-bearing mineral in the Huoshibulake pluton; the

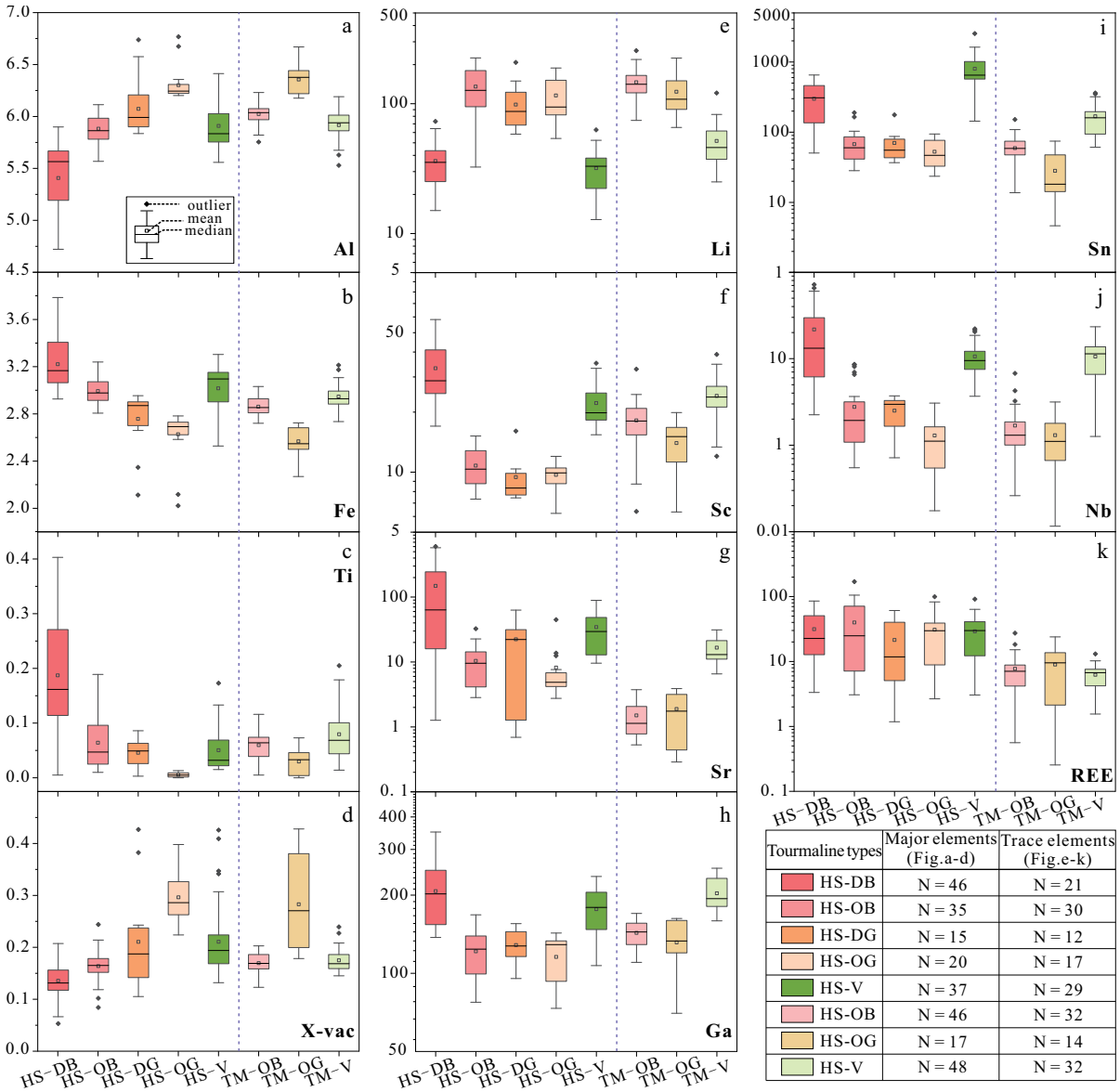

Tourmaline types	Major elements (Fig.a-d)	Trace elements (Fig.e-k)
HS-DB	N = 46	N = 21
HS-OB	N = 35	N = 30
HS-DG	N = 15	N = 12
HS-OG	N = 20	N = 17
HS-V	N = 37	N = 29
HS-OB	N = 46	N = 32
HS-OG	N = 17	N = 14
HS-V	N = 48	N = 32

Figure 8. Box plots showing comparisons of selected major element (apfu, **a**–**d**) and trace element (ppm, **e**–**k**) compositions in different tourmaline types from the Huoshibulake and Tamu plutons. The "N" values in the table are numbers of analyzed spots. Abbreviations are same as Figure 6. (Color online.)

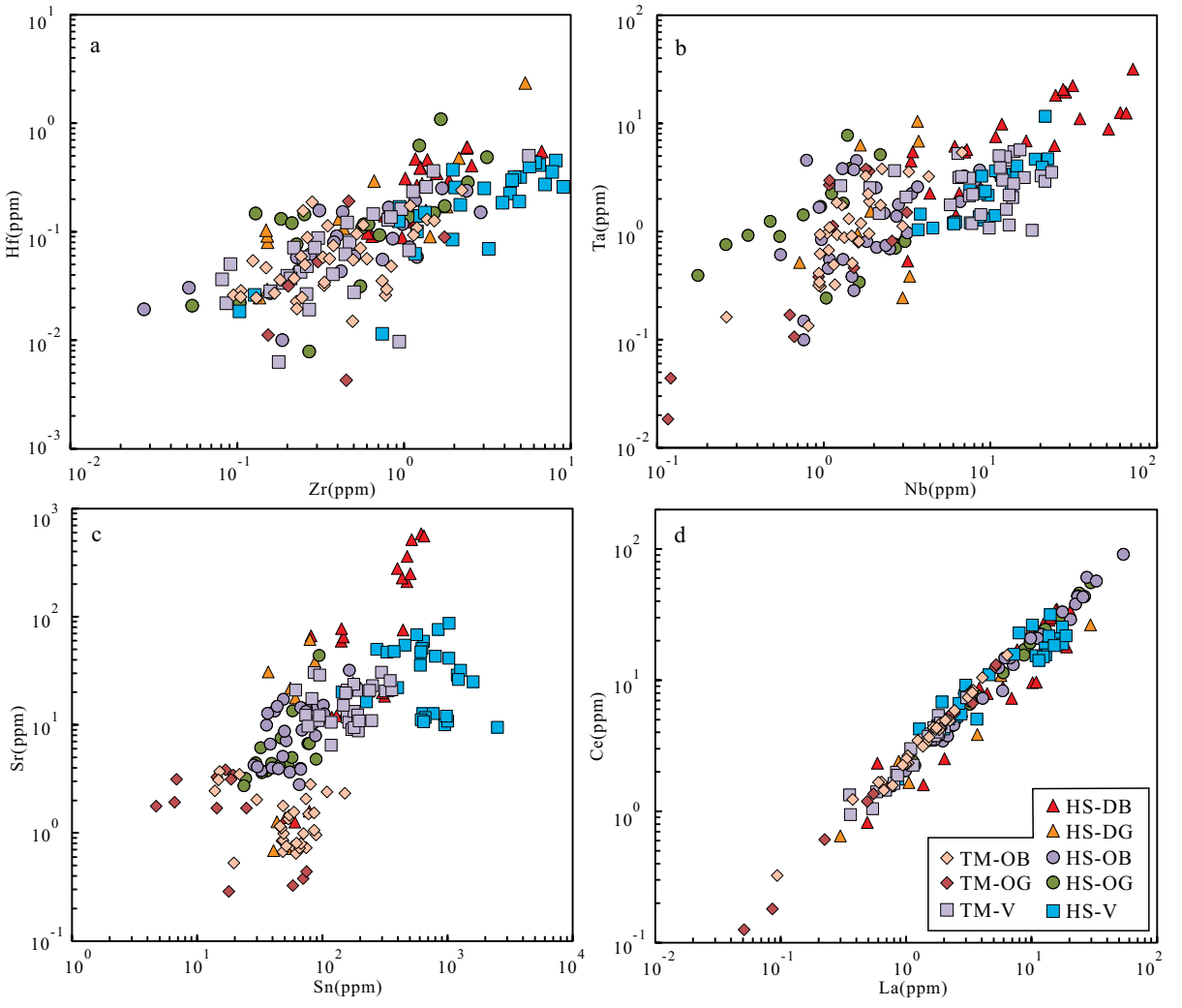

FIGURE 9. Trace element variation diagrams of tourmaline from the Huoshibulake and Tamu plutons, showing the positive correlations between different element pairs. Abbreviations are same as Figure 6. (Color online.)

lower Sr contents of the HS-OB (2.82–44.8 ppm) tourmaline compared to HS-DB ones (11.9–602 ppm) are consistent with the later formation of tourmaline-quartz orbicules. Overgrowths of green-blue tourmaline (HS-DG, HS-OG, and TM-OG types) around brown cores (HS-DB, HS-OB, and TM-OB types) show sharp changes in both elemental and B isotopic compositions, precluding progressive crystallization and revealing a change of the crystallization medium. Analogous characteristics have also been reported in highly evolved peraluminous granites and interpreted as the transition of tourmaline formation from a silicate melt-dominated to hydrothermal environments (e.g., Zhao et al. 2022; Drivenes et al. 2015; Trumbull et al. 2020). Compared with the brown tourmaline, the green-blue overgrowths exhibit lower Ca, Na, Ti, and Fe contents and higher X-site vacancy (Figs. 8a–8d). The significantly higher Sr and Sc and lower Li contents of the brown tourmaline than those of green-blue tourmaline (Figs. 8e–8g) agree with the preference of Sr and Sc to strongly partition into melt while Li is highly fluid mobile (Bai and Koster Van Groos 1999; Penniston-Dorland et al. 2012). Besides, the stronger B isotopic fractionation during crystallization of tourmaline from fluids than that from melts generally causes significantly heavier B isotopic compositions in hydrothermal tourmaline than in magmatic tourmaline (see details in the next section), consistent with the fractionation observed in this study (Fig. 10). In combination with its occurrence in both disseminated and orbicular tourmaline groups, the green-blue tourmaline is interpreted to have a hydrothermal origin and precipitated from later exsolved fluids in the magmatic-hydrothermal transition.

Both external fluid activity and exsolved magmatic-hydrothermal melt/fluid at the latest stage of magmatic evolution could account for tourmaline-quartz veins (Zhao et al. 2019). However, the extremely low Ca and Mg contents of the vein tourmaline argue against an external origin involving the country rocks, which mainly consist of calcareous sandstone and limestone (Shuai et al. 2019). The tourmaline-quartz veins in the Huoshibulake and Tamu plutons show straight and sharp boundaries with the host granite (Figs. 5a–5b). Most of these veins have near-vertical orientations and are generally paral-

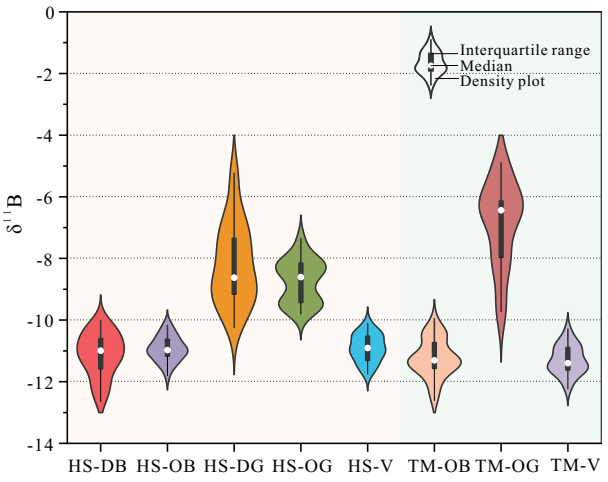

Figure 10. Box plots showing variations of boron isotopic compositions in different types of tourmaline. Abbreviations are same as Figure 6. (Color online.)

lel in the same outcrop (Fig. 5a), indicating that they intruded along fractures after the granites solidified. U-Pb dating of the cassiterite from the tourmaline-quartz vein yields a coeval age (271 ± 4 Ma) with the host granite (275 ± 2 Ma), suggesting that they formed within the same magmatic event (Wu et al. 2024). Besides, the indistinguishable elemental (Figs. 8 and 9) and B isotopic compositions (Fig. 10) of the vein tourmaline with the disseminated tourmaline permit a similar origin. Based on these lines of evidence, we propose that the tourmaline-quartz veins were probably the product of highly evolved, B-rich melts of another magma pulse from a deeper cogenetic magma chamber emplaced after the plutons had consolidated.

Boron source and variations of boron isotopes

The fractionation of B isotopes in magmatic-hydrothermal systems is commonly explained by differential B coordination in different phases since ^{11}B exhibits a greater tendency to trigonal coordination while ^{10}B adopts tetrahedral coordination (Kakihana et al. 1977; Palmer and Swihart 1996). Boron is predominately trigonally coordinated in tourmaline and aqueous fluid (Bassett 1976; Schmidt et al. 2005); by contrast, B coordination in silicate melt is a mix of both trigonal and tetrahedral coordination depending on water content, alkali/aluminum ratio, and speciation of aluminum (Dingwell et al. 1996). Thus, magmatic-hydrothermal processes involving phase separation (e.g., Rayleigh fractionation during the crystallization of tourmaline from melts or fluids and isotopic redistribution during melt/fluid exsolution) would be encoded as differential B isotopic fractionation (Smith and Yardley 1996).

Due to the lack of experimental determination, the B isotopic fractionation between silicate melt and tourmaline was generally calculated indirectly by combining fractionation between melt and fluid ($\Delta^{11}B_{melt–fluid}$) and fluid and tourmaline ($\Delta^{11}B_{Tur–fluid}$) in the past decades (e.g., Zhao et al. 2021a; Maner and London 2017). However, this method has significant uncertainty since (1) the available $\Delta^{11}B_{melt–fluid}$ and $\Delta^{11}B_{Tur–fluid}$ data were determined by different experimental methods (Cheng et al. 2022) and (2) the predicted B isotopic fractionation between granitic melt and tourmaline is much more significant when compared with that observed in the natural magmatic tourmaline (Kowalski and Wunder 2018; Zhao et al. 2022). Recently, Cheng et al. (2022) reported the first set of experimental data of B isotopic fractionation between granitic melt and tourmaline, which they defined as $\Delta^{11}B_{melt–Tur} = 4.51 \times (1000/T\,[K]) - 3.94$. Using the Titanium-in-quartz thermobarometer proposed by Huang and Audétat (2012), crystallization temperatures of the magmatic tourmaline paragenic with quartz from the Huoshibulake and Tamu plutons are estimated as 624–825 and 614–838 °C, respectively (Online Materials[1]). The small B isotopic fractionation between melt and magmatic tourmaline ($\Delta^{11}B_{melt–Tur} = –0.26$ at 800 °C and –1.23 at 600 °C) based on the empirical equation is consistent with the limited B isotopic variation observed in the magmatic tourmaline groups in this study (HS-DB, HS-OB, HS-V, TM-OB, and TM-V; Fig. 10). With increasing B concentration in the residual melt, immiscible B-rich magmatic globules could separate from coexisting granitic magma to form quartz-tourmaline orbicules (Balen and Broska 2011; Thomas et al. 2005). Gurenko et al. (2005) observed negligible fractionation between coexisting immiscible B-rich melt and silicate melt. This mechanism explains the similar B isotopic composition of magmatic tourmaline crystallized from silicate melt (HS-DB, 12.6 to –10.0‰) and those from conjugated aqueous B-rich melts (HS-OB, –11.8 to –10.2‰; TM-OB, –12.6 to –10.0‰). Considering the lightest $\delta^{11}B$ value of –12.6‰, the initial $\delta^{11}B$ value of the initial melt is set as –12.3‰. The modeling in Figure 11a shows that the slight rise of $\delta^{11}B$ values in the magmatic tourmaline can be reproduced by the combination of increasing $\delta^{11}B$ values in the residual melt caused by Rayleigh fractionation of tourmaline crystallization and the enlargement of $\Delta^{11}B_{melt–Tur}$ with decreasing temperature.

Both fluid exsolution and Rayleigh fractionation during the crystallization of hydrothermal tourmaline cause increasing $\delta^{11}B$ values in later crystallizing hydrothermal tourmaline. The experimental data reported by Hervig et al. (2002) suggested significant B isotopic fractionation between hydrous fluids and silicate melt of rhyolitic composition at high temperatures (up to −7.1‰, at 750 °C and 500 MPa). Hervig et al. (2002) explained the remarkable $\Delta^{11}B_{melt-fluid}$ by the significant difference of B coordination between melts (dominantly tetrahedral) and fluids (dominantly trigonal). However, this result and explanation have been long debated since they contradict the spectroscopic measurements on synthesized and natural silicate glasses, which show a small amount of, or negligible, tetrahedral B (Schmidt et al. 2004; Tonarini et al. 2003b). Both the experimental studies and the analysis of melt and fluid inclusions in evolved granites and pegmatites have revealed that the system changes from a melt-driven stage to a fluid-driven period at a near-solidus temperature of 500 °C (Thomas et al. 2003; Veksler et al. 2002). In this study, given the heaviest $\delta^{11}B$ values of –10.0‰ of the magmatic tourmaline and assuming the fluid exsolution temperature of 500 °C, the $\delta^{11}B$ value of the latest melt would be ~–8.1‰. For hydrothermal tourmaline, Meyer et al. (2008) proposed that the B isotopic fractionation between fluid and tourmaline is temperature-dependent and can be calculated by $\Delta^{11}B_{tour-fluid} = –4.20 \times [1000/T\,(K)] + 3.52$. Considering the most negative $\delta^{11}B$ value recorded by HS-DG (–10.2‰) and assuming the exsolution temperature of 500 °C, the $\delta^{11}B$ value of initial hydrothermal

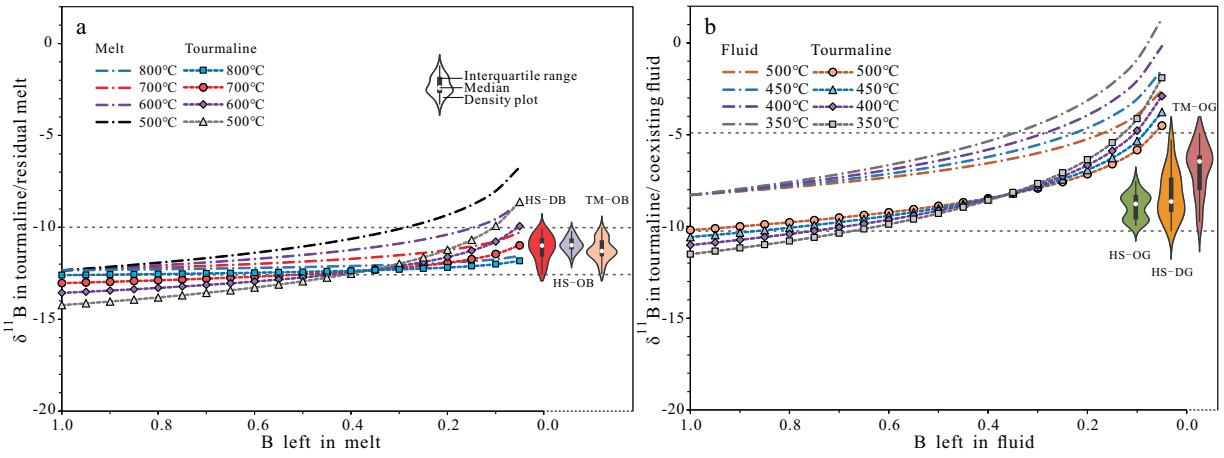

Figure 11. Modeling of B isotopic fractionation between (**a**) melt and tourmaline and (**b**) fluid and tourmaline. The initial $\delta^{11}B$ values of the melt and aqueous fluid are set as –12.3 and –8.3‰, respectively. See text for details. The violin plots show the ranges of B isotopic compositions of different tourmaline types. Abbreviations are same as Figure 6. (Color online.)

fluid in equilibrium with the late green-blue tourmaline would be about –8.3‰. The near-identical estimated B isotopic compositions between the residual melt and the initial fluid imply that the B isotopic fractionation during fluid exsolution in the studied samples is negligible. Alternatively, the Rayleigh fractionation modeling shown in Figure 11b demonstrates that the heavy and highly variable B isotopic composition of the hydrothermal green-blue tourmaline can be explained by significant Rayleigh fractionation during the depletion of B in the fluid. The decrease in temperature can amplify the fluid-tourmaline B isotopic fractionation, and the heaviest composition (–4.9‰ from the TM-OG) can be achieved by ~86% depletion of B in the residual fluid at 400 °C (Fig. 11b).

In summary, the B isotopic variations in the magmatic and hydrothermal tourmaline observed in the Huoshibulake and Tamu plutons can be reproduced by the Rayleigh fractionation during the magmatic-hydrothermal transition. Based on the discussion above, an idealized model is proposed and illustrated in Figure 12.

Rare-metal concentration and precipitation during the magmatic-hydrothermal transition in granitic systems

The magmatic-hydrothermal transition has been considered one of the most critical stages in the granite-related metallogenic system, during which rare metals generally reach their peak concentrations and precipitate as economic minerals (Kaeter et al. 2018; Ballouard et al. 2020). However, whether the rare metal mineralization in the granitic system occurs at the melt-driven or fluid-driven stage is still widely disputed (Ballouard et al. 2016; Sokół et al. 2022; Yang et al. 2020). Some previous studies highlighted the role of high-degree fractional crystallization and suggested that the ore-forming elements are highly concentrated and deposited in the residual melts at the end of the magmatic period (Borodulin et al. 2009; Chevychelov et al. 2005). In contrast, some studies argued that melt-melt immiscibility or fluid exsolution during the magmatic-hydrothermal transition could be a critical mechanism for the hyper-enrichment of rare metals (Ballouard et al. 2016; Thomas and Davidson 2016), especially when the strongly differentiated distribution of fluxing elements is involved (Mohamed 2013; Vasyukova and Williams-Jones 2014). For instance, some experimental studies suggested that Nb, Ta, and REE can form complexes with ligands (e.g., F^-, Cl^-) through which they can be effectively concentrated in aqueous melts or hydrothermal fluids (Migdisov and Williams-Jones 2014; Timofeev et al. 2015; Zaraisky et al. 2010). However, little direct evidence from natural systems has been found to confirm trace element distribution behavior during the latest melt-fluid interaction in the granitic systems.

The characteristics of B-rich melt/fluid exsolution in this study provide a unique insight into the rare metal mineralization during the magmatic-hydrothermal transition. In the Huoshibulake pluton, HS-DB tourmaline (interpreted as early magmatic) exhibits high Nb (2.25–71.7 ppm, with an average of 21.7 ppm) and Ta (0.52–31.6 ppm, with an average of 9.20 ppm) contents. In comparison, those of HS-OB type crystallized from immiscible aqueous melt and HS-DG and HS-OG crystallized from exsolved fluid have significantly lower Nb and Ta contents (Fig. 8j). The compositional variations of tourmaline are consistent with the petrographic observations, that is, columbite is commonly observed, and paragenetic, with disseminated tourmaline while absent in the tourmaline–quartz orbicules. It is thereby inferred that Nb and Ta reached peak concentrations during the latest magmatic stage but were depleted in the exsolved aqueous B-rich melt/fluid in the Huoshibulake case. Similar compositional variations were also reported in tourmaline from the Shangbao Nb-Ta granite, South China (Zhao et al. 2021b). Unfortunately, the REE contents in the different types of tourmaline from the two mineralized plutons exhibit low and variable contents (Fig. 8k), providing limited information about their evolution and preference for melts or fluids. However, rare-earth minerals (e.g., monazite, fluocerite, and synchysite) are commonly observed in the granite matrix (Figs. 3a–3c) and the tourmaline-quartz veins (Figs. 3d–3f) and are rare in tourmaline-quartz orbicules, precluding the extraction effect of REE during aqueous B-rich melt/fluid exsolution. The Sn content in tourmaline has been widely employed to predict Sn mineralization potential due

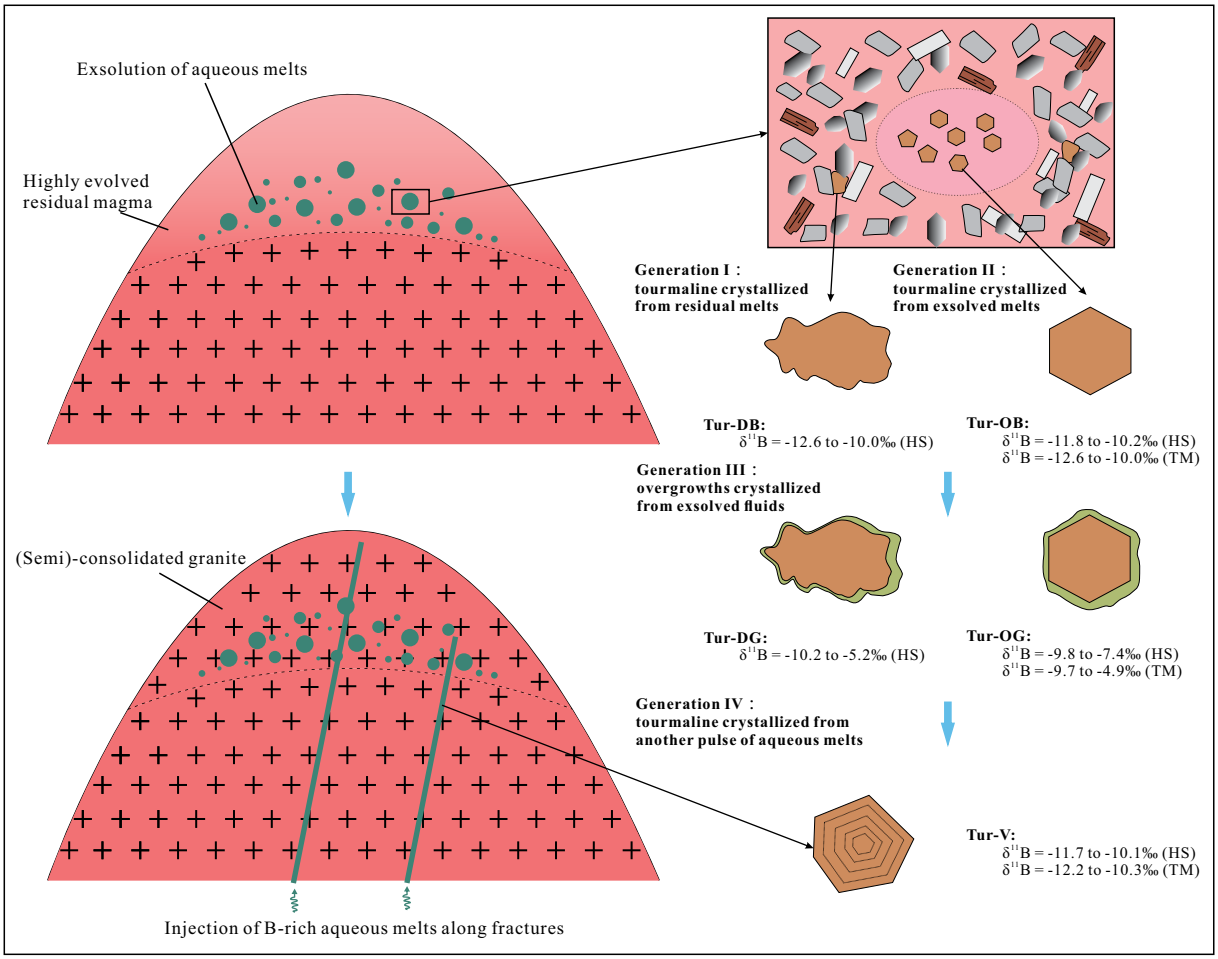

Figure 12. Idealized scenarios showing the formation of the different types of tourmaline. Generation I: during the late-stage crystallization of the plutons, B reached saturation and crystallized as disseminated tourmaline. Generation II: with continuous crystallization, the immiscibility of B-rich aqueous melts resulted in the crystallization of orbicular tourmaline. Generation III: exsolved fluids formed the overgrowths of tourmaline at the rims of the earlier magmatic tourmaline. Generation IV: another pulse of B-rich aqueous melts intruded into fractures of the consolidated granite. Abbreviations are same as Figure 6. (Color online.)

to its high partition coefficient (Hong et al. 2017; Qiu et al. 2021). In our case, tourmaline from the orbicules (HS-OB and HS-OG) and rim of disseminated tourmaline (HS-DG) show significantly lower Sn contents compared to the HS-DB (Fig. 8i), also arguing against the Sn enrichment in the B-rich melt and fluid phases during their exsolution. From this perspective, B-rich melt/fluid exsolution does not necessarily contribute to rare-metal mineralization.

As discussed above, the tourmaline-quartz orbicules resulted from exsolved B-rich melts in the late-stage crystallization of the Huoshibulake and Tamu granitic magmas, and the tourmaline-quartz veins represent another B-rich melt pulse from a deeper cogenetic magma chamber, both of them are regarded as the products of the magmatic-hydrothermal transition. However, a notable phenomenon is that the veins exhibit considerably higher Nb, Ta, Sn, and REE on both the bulk rock and the tourmaline scales (except for REE in tourmaline), with a higher abundance of rare-metal minerals compared to the orbicules. These rare-metal minerals show close paragenesis with fluorite, especially acicular synchysite that only occurs as inclusions in fluorite (Figs. 3d–3f), linking fluorite saturation with REE and Nb precipitation. The relevance of fluorine and rare metals is also supported by the significantly higher whole-rock F, Nb, and ΣREE contents [1.10 wt%, 233 ppm, and 831 ppm, respectively (Wu et al. 2024)] of the tourmaline-quartz vein compared to those of the tourmaline-quartz orbicule (0.20 wt%, 84.9 ppm, and 208 ppm, respectively). These lines of evidence indicate that the timing when fluorite reaches saturation is a critical factor in determining the concentration and precipitation of rare metals during the magmatic-hydrothermal process. Fluorine is considered an important agent for transporting Nb and REE as fluoride species (Williams-Jones et al. 2000; Ruberti et al. 2008). Thus, the saturation of fluorite can cause rapid depletion of the complexing ligand and simultaneously trigger the precipitation of these rare metals (Smith and Henderson 2000). During the crystallization of the Huoshibulake and Tamu plutons, fluorite saturation occurred at a relatively early stage of the magmatic-hydrothermal transition and resulted in the disseminated crystallization of rare metals in

the granite matrix; in contrast, fluorine in the parental magmas of the tourmaline-quartz veins was concentrated, and fluorite did not reach saturation until their emplacement, leading to the veined rare-metal mineralization after B-rich melts exsolution.

Implications

This study recognizes four generations of tourmaline formed from late magmatic, through the magmatic-hydrothermal transition, to late hydrothermal stages in the Huoshibulake and Tamu alkali granites. The petrographic, compositional, and B isotopic variations recorded by the tourmaline provide valuable information for investigating the magmatic-hydrothermal processes. This study highlights the use of tourmaline as a tracer to unravel the magmatic-hydrothermal transition and related rare-metal mineralization in granitic systems. For instance, the differential rare-metal abundances between tourmalines from orbicules and veins are in good accordance with rare-metal mineral abundance. These observations, together with the close paragenesis of ore minerals and fluorite, further highlight the critical role of fluorite saturation in rare-metal enrichment and mineralization during the transition. It is also important to note that when employing the compositional index of tourmaline (e.g., Sn, which has been commonly used) to evaluate metallogenic potential, extra attention should be paid to the mineral structure and multi-generation crystallization.

Acknowledgments and funding

We thank Bei-Bei Pan and Hai-Zhou Li for their assistance during fieldwork. We extend our thanks to Yong-Jun Zhao, Kui-Dong Zhao, He-Dong Zhao, Di Zhang, and Chao Li for their help during the EPMA and LA-MC-ICP-MS analysis. We appreciate Andrea Dini and two anonymous reviewers for their insightful comments. We are grateful to chief editor Don Baker and associate editor Paul Tomascak for their guidance and support throughout the review process.

This work was financially supported by National Natural Science Foundation of China (NSFC grant nos. 42173052 and 92162322) and Natural Science Basic Research Program of Shaanxi (grant nos. 2023-JC-QN-0345 and 2023-JC-YB-241). The visit of Huanhuan Wu at University of St Andrews was funded by the China Scholarship Council (no. 202206400021).

References cited

Audétat, A., Garbe-Schönberg, D., Kronz, A., Pettke, T., Rusk, B., Donovan, J.J., and Lowers, H.A. (2015) Characterisation of a natural quartz crystal as a reference material for microanalytical determination of Ti, Al, Li, Fe, Mn, Ga and Ge. Geostandards and Geoanalytical Research, 39, 171–184.

Bai, T.B. and Koster Van Groos, A.F. (1999) The distribution of Na, K, Rb, Sr, Al, Ge, Cu, W, Mo, La, and Ce between granitic melts and coexisting aqueous fluids. Geochimica et Cosmochimica Acta, 63, 1117–1131, https://doi.org/10.1016/S0016-7037(98)00284-1.

Balen, D. and Broska, I. (2011) Tourmaline nodules: Products of devolatilization within the final evolutionary stage of granitic melt? Special Publication—Geological Society of London, 350, 53–68, https://doi.org/10.1144/SP350.4.

Ballouard, C., Poujol, M., Boulvais, P., Branquet, Y., Tartèse, R., and Vigneresse, J.L. (2016) Nb-Ta fractionation in peraluminous granites: A marker of the magmatic-hydrothermal transition. Geology, 44, 231–234, https://doi.org/10.1130/G37475.1.

Ballouard, C., Massuyeau, M., Elburg, M.A., Tappe, S., Viljoen, F., and Brandenburg, J.T. (2020) The magmatic and magmatic-hydrothermal evolution of felsic igneous rocks as seen through Nb-Ta geochemical fractionation, with implications for the origins of rare-metal mineralizations. Earth-Science Reviews, 203, 103115, https://doi.org/10.1016/j.earscirev.2020.103115.

Bassett, R.L. (1976) The geochemistry of boron in thermal waters, 307 p. Ph.D. thesis, Stanford University.

Borodulin, G.P., Chevychelov, V.Y., and Zaraysky, G.P. (2009) Experimental study of partitioning of tantalum, niobium, manganese, and fluorine between aqueous fluoride fluid and granitic and alkaline melts. Doklady Earth Sciences, 427, 868–873, https://doi.org/10.1134/S1028334X09050341.

Carr, P., Norman, M.D., Bennett, V.C., and Blevin, P.L. (2021) Tin enrichment in magmatic-hydrothermal environments associated with cassiterite mineralization at Ardlethan, Eastern Australia: Insights from Rb-Sr and Sm-Nd isotope compositions in tourmaline. Economic Geology and the Bulletin of the Society of Economic Geologists, 116, 147–167, https://doi.org/10.5382/econgeo.4774.

Chen, F.W., Li, H.Q., and Lu, Y.F. (2002) Temporo-spatial distribution of rare metal and REE deposits in Xinjiang, Northwest China. Acta Geologica Sinica—English Edition, 76, 478–487, https://doi.org/10.1111/j.1755-6724.2002.tb00101.x.

Cheng, Z.G., Zhang, Z.C., Aibai, A., Kong, W.L., and Holtz, F. (2018) The role of magmatic and post-magmatic hydrothermal processes on rare-earth element mineralization: A study of the Bachu carbonatites from the Tarim Large Igneous Province, NW China. Lithos, 314–315, 71–87, https://doi.org/10.1016/j.lithos.2018.05.023.

Cheng, L., Zhang, C., Zhou, Y., Horn, I., Weyer, S., and Holtz, F. (2022) Experiments reveal enrichment of ^{11}B in granitic melt resulting from tourmaline crystallisation. Geochemical Perspectives Letters, 20, 37–42, https://doi.org/10.7185/geochemlet.2206.

Chevychelov, V.Y., Zaraisky, G.P., Borisovskii, S.E., and Borkov, D.A. (2005) Effect of melt composition and temperature on the partitioning of Ta, Nb, Mn, and F between granitic (alkaline) melt and fluorine-bearing aqueous fluid: Fractionation of Ta and Nb and conditions of ore formation in rare-metal granites. Petrology, 13, 305–321.

Cui, J.Q., Yang, S.Y., Jiang, S.Y., and Xie, J. (2019) Improved accuracy for trace element analysis of Al and Ti in quartz by electron probe microanalysis. Microscopy and Microanalysis, 25, 47–57.

Cui, J.Q., Guo, S.B., Zhang, R.X., Xie, J., and Yang, S.Y. (2021) EPMA simultaneous determination of an element by multi-spectrometer: A case study of the determination of Al and Ti contents in quartz. Geological Journal of China Universities, 27, 340.

Dingwell, D.B., Pichavant, M., and Holtz, F. (1996) Experimental studies of boron in granitic melts. In L.M. Anovitz and E.S. Grew, Eds., Boron, 33, 331–386. Reviews in Mineralogy and Geochemistry, Mineralogical Society of America, Chantilly, Virginia.

Drivenes, K., Larsen, R.B., Müller, A., Sørensen, B.E., Wiedenbeck, M., and Raanes, M.P. (2015) Late-magmatic immiscibility during batholith formation: Assessment of B isotopes and trace elements in tourmaline from the Land's End granite, SW England. Contributions to Mineralogy and Petrology, 169, 56, https://doi.org/10.1007/s00410-015-1151-6.

Dutrow, B.L. and Henry, D.J. (2011) Tourmaline: A geologic DVD. Elements, 7, 301–306, https://doi.org/10.2113/gselements.7.5.301.

Dyar, M.D., Wiedenbeck, M., Robertson, D., Cross, L.R., Delaney, J.S., Ferguson, K., Francis, C.A., Grew, E.S., Guidotti, C.V., Hervig, R.L., and others. (2001) Reference minerals for the microanalysis of light elements. Geostandards Newsletter, 25, 441–463, https://doi.org/10.1111/j.1751-908X.2001.tb00616.x.

Gao, J., Klemd, R., Qian, Q., Zhang, X., Li, J., Jiang, T., and Yang, Y. (2011) The collision between the Yili and Tarim blocks of the Southwestern Altaids: Geochemical and age constraints of a leucogranite dike crosscutting the HPLT metamorphic belt in the Chinese Tianshan Orogen. Tectonophysics, 499, 118–131.

Gurenko, A.A., Veksler, I.V., Meixner, A., Thomas, R., Dorfman, A.M., and Dingwell, D.B. (2005) Matrix effect and partitioning of boron isotopes between immiscible Si-rich and B-rich liquids in the Si-Al-B-Ca-Na-O system: A SIMS study of glasses quenched from centrifuge experiments. Chemical Geology, 222, 268–280, https://doi.org/10.1016/j.chemgeo.2005.07.004.

Halter, W.E. and Webster, J.D. (2004) The magmatic to hydrothermal transition and its bearing on ore-forming systems. Chemical Geology, 210, 1–6, https://doi.org/10.1016/j.chemgeo.2004.06.001.

Harlaux, M., Kouzmanov, K., Gialli, S., Laurent, O., Rielli, A., Dini, A., Chauvet, A., Menzies, A., Kalinaj, M., and Fontboté, L. (2020) Tourmaline as a tracer of late-magmatic to hydrothermal fluid evolution: The world-class San Rafael Tin (-Copper) Deposit, Peru. Economic Geology and the Bulletin of the Society of Economic Geologists, 115, 1665–1697, https://doi.org/10.5382/econgeo.4762.

Henry, D.J. and Dutrow, B.L. (1990) Ca substitution in Li-poor aluminous tourmaline. Canadian Mineralogist, 28, 111–124.

——— (2012) Tourmaline at diagenetic to low-grade metamorphic conditions: Its petrologic applicability. Lithos, 154, 16–32, https://doi.org/10.1016/j.lithos.2012.08.013.

Henry, D.J. and Guidotti, C.V. (1985) Tourmaline as a petrogenetic indicator mineral: An example from the staurolite-grade metapelites of NW Maine. American Mineralogist, 70, 1–15.

Henry, D.J., Novak, M., Hawthorne, F.C., Ertl, A., Dutrow, B.L., Uher, P., and Pezzotta, F. (2011) Nomenclature of the tourmaline-supergroup minerals. American Mineralogist, 96, 895–913, https://doi.org/10.2138/am.2011.3636.

Hervig, R.L., Moore, G.M., Williams, L.B., Peacock, S.M., Holloway, J.R., and Roggensack, K. (2002) Isotopic and elemental partitioning of boron between hydrous fluid and silicate melt. American Mineralogist, 87, 769–774, https://doi.org/10.2138/am-2002-5-620.

Hong, W., Cooke, D.R., Zhang, L.J., Fox, N., and Thompson, J. (2017) Tourmaline-rich features in the Heemskirk and Pieman Heads granites from western Tasmania, Australia: Characteristics, origins, and implications for tin mineralization. American Mineralogist, 102, 876–899, https://doi.org/10.2138/am-2017-5838.

Hong, W., Fox, N., Cooke, D.R., Zhang, L.J., and Fayek, M. (2020) B- and O-isotopic compositions of tourmaline constrain late-stage magmatic volatile exsolution in Tasmanian tin-related granite systems. Mineralium Deposita, 55, 63–78, https://doi.org/10.1007/s00126-019-00885-5.

Hou, K.J., Li, Y.H., Xiao, Y.K., Liu, F., and Tian, Y.R. (2010) In situ boron isotope measurements of natural geological materials by LA-MC-ICP-MS. Chinese Science Bulletin, 55, 3305–3311, https://doi.org/10.1007/s11434-010-4064-9.

Huang, R.F. and Audétat, A. (2012) The titanium-in-quartz (TitaniQ) thermobarometer: A critical examination and re-calibration. Geochimica et Cosmochimica Acta, 84, 75–89, https://doi.org/10.1016/j.gca.2012.01.009.

Huang, H., Zhang, Z.C., Kusky, T., Santosh, M., Zhang, S., Zhang, D.Y., Liu, J.L., and Zhao, Z.D. (2012) Continental vertical growth in the transitional zone between South Tianshan and Tarim, western Xinjiang, NW China: Insight from the Permian Halajun A1-type granitic magmatism. Lithos, 155, 49–66, https://doi.org/10.1016/j.lithos.2012.08.014.

Huang, H., Zhang, Z.C., Santosh, M., Zhang, D.Y., and Wang, T. (2015) Petrogenesis of the Early Permian volcanic rocks in the Chinese South Tianshan: Implications for crustal growth in the Central Asian Orogenic Belt. Lithos, 228–229, 23–42, https://doi.org/10.1016/j.lithos.2015.04.017.

Huang, H., Wang, T., Zhang, Z.C., Li, C., and Qin, Q. (2018) Highly differentiated fluorine-rich, alkaline granitic magma linked to rare metal mineralization: A case study from the Boziguo'er rare metal granitic pluton in South Tianshan Terrane, Xinjiang, NW China. Ore Geology Reviews, 96, 146–163, https://doi.org/10.1016/j.oregeorev.2018.04.021.

Jiang, S.Y., Yu, J.M., and Lu, J.J. (2004) Trace and rare-earth element geochemistry in tourmaline and cassiterite from the Yunlong tin deposit, Yunnan, China: Implication for migmatitic-hydrothermal fluid evolution and ore genesis. Chemical Geology, 209, 193–213, https://doi.org/10.1016/j.chemgeo.2004.04.021.

Kaeter, D., Barros, R., Menuge, J.F., and Chew, D.M. (2018) The magmatic–hydrothermal transition in rare-element pegmatites from southeast Ireland: LA-ICP-MS chemical mapping of muscovite and columbite-tantalite. Geochimica et Cosmochimica Acta, 240, 98–130, https://doi.org/10.1016/j.gca.2018.08.024.

Kakihana, H., Kotaka, M., Satoh, S., Nomura, M., and Okamoto, M. (1977) Fundamental studies on the ion-exchange separation of boron isotopes. Bulletin of the Chemical Society of Japan, 50, 158–163, https://doi.org/10.1246/bcsj.50.158.

Kowalski, P.M., and Wunder, B. (2018) Boron isotope fractionation among vapor-liquids-solids-melts: Experiments and atomistic modeling. In H. Marschall and G. Foster, Eds., Advances in Geochemistry: Boron Isotopes: The Fifth Element, 7, p. 33–69. Springer.

Linnen, R.L., Samson, I.M., Williams-Jones, A.E., and Chakhmouradian, A.R. (2014) Geochemistry of the rare-earth element, Nb, Ta, Hf, and Zr deposits. Treatise on Geochemistry, 13, 543–568, https://doi.org/10.1016/B978-0-08-095975-7.01124-4.

Liu, T. and Jiang, S.Y. (2021) Multiple generations of tourmaline from Yushishanxi leucogranite in South Qilian of western China record a complex formation history from B-rich melt to hydrothermal fluid. American Mineralogist, 106, 994–1008, https://doi.org/10.2138/am-2021-7473.

Liu, Y.S., Hu, Z.C., Zong, K.Q., Gao, C.G., Gao, S., Xu, J., and Chen, H.H. (2010) Reappraisement and refinement of zircon U-Pb isotope and trace element analyses by LA-ICP-MS. Chinese Science Bulletin, 55, 1535–1546, https://doi.org/10.1007/s11434-010-3052-4.

Long, Z.Y., Yu, X.Y., and Zheng, Y.Y. (2021) Ore formation of the Dayakou emerald deposit (Southwest China) constrained by chemical and boron isotopic composition of tourmaline. Ore Geology Reviews, 135, 104208, https://doi.org/10.1016/j.oregeorev.2021.104208.

Maner, J.L. IV and London, D. (2017) The boron isotopic evolution of the Little Three pegmatites, Ramona, CA. Chemical Geology, 460, 70–83, https://doi.org/10.1016/j.chemgeo.2017.04.016.

Meyer, C., Wunder, B., Meixner, A., Romer, R.L., and Heinrich, W. (2008) Boron-isotope fractionation between tourmaline and fluid: An experimental re-investigation. Contributions to Mineralogy and Petrology, 156, 259–267, https://doi.org/10.1007/s00410-008-0285-1.

Michaud, J.A.-S. and Pichavant, M. (2020) Magmatic fractionation and the magmatic-hydrothermal transition in rare metal granites: Evidence from Argemela (Central Portugal). Geochimica et Cosmochimica Acta, 289, 130–157, https://doi.org/10.1016/j.gca.2020.08.022.

Migdisov, A.A. and Williams-Jones, A.E. (2014) Hydrothermal transport and deposition of the rare earth elements by fluorine-bearing aqueous liquids. Mineralium Deposita, 49, 987–997, https://doi.org/10.1007/s00126-014-0554-z.

Mohamed, M.A.M. (2013) Immiscibilty between silicate magma and aqueous fluids in Egyptian rare-metal granites: Melt and fluid inclusions study. Arabian Journal of Geosciences, 6, 4021–4033, https://doi.org/10.1007/s12517-012-0664-9.

Nechaev, V.P., Dai, S., Zhao, L., Moore, T.A., and Nechaeva, E.V. (2021) The Tarim Basin, China, a prospect for plume-related Zr(Hf)-Nb(Ta)-REY-Ga-U mineralization. Ore Geology Reviews, 133, 104081, https://doi.org/10.1016/j.oregeorev.2021.104081.

Palmer, M.R. and Swihart, G.H. (1996) Boron isotope geochemistry: an overview. In E.S. Grew and L.M. Anovitz, Eds., Boron, 33, 709–744. Reviews in Mineralogy and Geochemistry, Mineralogical Society of America, Chantilly, Virginia.

Penniston-Dorland, S.C., Bebout, G.E., Pogge von Strandmann, P.A.E., Elliott, T., and Sorensen, S.S. (2012) Lithium and its isotopes as tracers of subduction zone fluids and metasomatic processes: Evidence from the Catalina Schist, California, U.S.A. Geochimica et Cosmochimica Acta, 77, 530–545, https://doi.org/10.1016/j.gca.2011.10.038.

Qiu, K.F., Yu, H.C., Hetherington, C., Huang, Y.Q., Yang, T., and Deng, J. (2021) Tourmaline composition and boron isotope signature as a tracer of magmatic-hydrothermal processes. American Mineralogist, 106, 1033–1044, https://doi.org/10.2138/am-2021-7495.

Rozendaal, A. and Bruwer, L. (1995) Tourmaline nodules: Indicators of hydrothermal alteration and Sn-Zn-(W) mineralization in the Cape Granite Suite, South Africa. Journal of African Earth Sciences, 21, 141–155, https://doi.org/10.1016/0899-5362(95)00088-B.

Ruberti, E., Enrich, G.E., Gomes, C.B., and Comin-Chiaramonti, P. (2008) Hydrothermal REE fluorocarbonate mineralization at Barra do Itapirapua, a multiple stockwork carbonatite, Southern Brazil. Canadian Mineralogist, 46, 901–914, https://doi.org/10.3749/canmin.46.4.901.

Schmidt, B.C., Zotov, N., and Dupree, R. (2004) Structural implications of water and boron dissolution in albite glass. Journal of Non-Crystalline Solids, 337, 207–219, https://doi.org/10.1016/j.jnoncrysol.2004.04.007.

Schmidt, B.C., Thomas, R., and Heinrich, W. (2005) Boron speciation in aqueous fluids at 22 to 600 °C and 0.1 MPa to 2 GPa. Geochimica et Cosmochimica Acta, 69, 275–281, https://doi.org/10.1016/j.gca.2004.06.018.

Sheard, E.R., Williams-Jones, A.E., Heiligmann, M., Pederson, C., and Trueman, D.L. (2012) Controls on the concentration of zirconium, niobium, and the rare earth elements in the Thor Lake rare metal deposit, Northwest Territories, Canada. Economic Geology and the Bulletin of the Society of Economic Geologists, 107, 81–104, https://doi.org/10.2113/econgeo.107.1.81.

Shi, P.C. (2010) Alkali-rich intrusive rocks and their metallogenic characteristics in Zambile area, Tianshan Mountain, southwest Xinjiang. Xinjiang Nonferrous Metals, 33, 1–5.

Shuai, L., Liu, Z.Q., Tang, H., Yu, Z.C., and Jia, T. (2019) Report of 1:50,000 Mineral Geological Survey Results in Huoshibulake Area, Atushi City, Xinjiang (in Chinese), 290 p. Non-ferrous minerals Geological Survey Center, China.

Slack, J.F. (1996) Tourmaline associations with hydrothermal ore deposits. In E.S. Grew and L.M. Anovitz, Eds., Boron, 559–644. Reviews in Mineralogy and Geochemistry, Mineralogical Society of America, Chantilly, Virginia.

Slack, J.F. and Trumbull, R.B. (2011) Tourmaline as a recorder of ore-forming processes. Elements, 7, 321–326, https://doi.org/10.2113/gselements.7.5.321.

Smith, M.P. and Henderson, P. (2000) Preliminary fluid inclusion constraints on fluid evolution in the Bayan Obo Fe-REE-Nb deposit, Inner Mongolia, China. Economic Geology and the Bulletin of the Society of Economic Geologists, 95, 1371–1388, https://doi.org/10.2113/gsecongeo.95.7.1371.

Smith, M.P. and Yardley, B.W.D. (1996) The boron isotopic composition of tourmaline as a guide to fluid processes in the southwestern England orefield: An ion microprobe study. Geochimica et Cosmochimica Acta, 60, 1415–1427, https://doi.org/10.1016/0016-7037(96)00007-5.

Sokół, K., Finch, A.A., Hutchison, W., Cloutier, J., Borst, A.M., and Humphreys, M.C.S. (2022) Quantifying metasomatic high-field-strength and rare-earth element transport from alkaline magmas. Geology, 50, 305–310, https://doi.org/10.1130/G49471.1.

Thomas, R. and Davidson, P. (2016) Revisiting complete miscibility between silicate melts and hydrous fluids, and the extreme enrichment of some elements in the supercritical state—Consequences for the formation of pegmatites and ore deposits. Ore Geology Reviews, 72, 1088–1101, https://doi.org/10.1016/j.oregeorev.2015.10.004.

Thomas, R., Förster, H.J., and Heinrich, W. (2003) The behaviour of boron in a peraluminous granite-pegmatite system and associated hydrothermal solutions: A melt and fluid-inclusion study. Contributions to Mineralogy and Petrology, 144, 457–472, https://doi.org/10.1007/s00410-002-0410-5.

Thomas, R., Förster, H-J., Rickers, K., and Webster, J.D. (2005) Formation of extremely F-rich hydrous melt fractions and hydrothermal fluids during differentiation of highly evolved tin-granite magmas: A melts/fluids-inclusion study. Contributions to Mineralogy and Petrology, 148, 582–601, https://doi.org/10.1007/s00410-004-0624-9.

Thomas, R., Davidson, P., and Beurlen, H. (2012) The competing models for the origin and internal evolution of granitic pegmatites in the light of melt and fluid inclusion research. Mineralogy and Petrology, 106, 55–73, https://doi.org/10.1007/s00710-012-0212-z.

Timofeev, A., Migdisov, A.A., and Williams-Jones, A.E. (2015) An experimental study of the solubility and speciation of niobium in fluoride-bearing aqueous solutions at elevated temperature. Geochimica et Cosmochimica Acta, 158, 103–111, https://doi.org/10.1016/j.gca.2015.02.015.

Tonarini, S., Pennisi, M., Adorni-Braccesi, A., Dini, A., Ferrara, G., Gonfiantini, R., Wiedenbeck, M., and Gröning, M. (2003a) Intercomparison of boron isotope and concentration measurements. Part I: Selection, preparation and homogeneity tests of the intercomparison materials. Geostandards Newsletter, 27, 21–39, https://doi.org/10.1111/j.1751-908X.2003.tb00710.x.

Tonarini, S., Forte, C., Petrini, R., and Ferrara, G. (2003b) Melt/biotite $^{11}B/^{10}B$

isotopic fractionation and the boron local environment in the structure of volcanic glasses. Geochimica et Cosmochimica Acta, 67, 1863–1873, https://doi.org/10.1016/S0016-7037(02)00987-0.
Trumbull, R.B. and Chaussidon, M. (1999) Chemical and boron isotopic composition of magmatic and hydrothermal tourmalines from the Sinceni granite–pegmatite system in Swaziland. Chemical Geology, 153, 125–137, https://doi.org/10.1016/S0009-2541(98)00155-7.
Trumbull, R.B., and Slack, J.F. (2018) Boron isotopes in the continental crust: Granites, pegmatites, felsic volcanic rocks, and related ore deposits. In H. Marschall and G. Foster, Eds., Advances in Geochemistry: Boron Isotopes: The Fifth Element, 7, p. 249–272, Springer.
Trumbull, R.B., Krienitz, M.S., Gottesmann, B., and Wiedenbeck, M. (2007) Chemical and boron-isotope variations in tourmalines from an S-type granite and its source rocks: The Erongo granite and tourmalinites in the Damara Belt, Namibia. Contributions to Mineralogy and Petrology, 155, 1–18, https://doi.org/10.1007/s00410-007-0227-3.
Trumbull, R.B., Codeço, M.S., Jiang, S.Y., Palmer, M.R., and Slack, J.F. (2020) Boron isotope variations in tourmaline from hydrothermal ore deposits: A review of controlling factors and insights for mineralizing systems. Ore Geology Reviews, 125, 103682, https://doi.org/10.1016/j.oregeorev.2020.103682.
van Hinsberg, V.J., Henry, D.J., and Dutrow, B.L. (2011) Tourmaline as a petrologic forensic mineral: A unique recorder of its geologic past. Elements, 7, 327–332, https://doi.org/10.2113/gselements.7.5.327.
Vasyukova, O. and Williams-Jones, A.E. (2014) Fluoride–silicate melt immiscibility and its role in REE ore formation: Evidence from the Strange Lake rare metal deposit, Québec-Labrador, Canada. Geochimica et Cosmochimica Acta, 139, 110–130, https://doi.org/10.1016/j.gca.2014.04.031.
Veksler, I.V., Thomas, R., and Schmidt, C. (2002) Experimental evidence of three coexisting immiscible fluids in synthetic granitic pegmatite. American Mineralogist, 87, 775–779, https://doi.org/10.2138/am-2002-5-621.
Wei, X., Xu, Y.G., He, B., Zhang, L., Xia, X.P., and Shi, X.F. (2019) Zircon U-Pb age and Hf-O isotope insights into genesis of Permian Tarim felsic rocks, NW China: Implications for crustal melting in response to a mantle plume. Gondwana Research, 76, 290–302, https://doi.org/10.1016/j.gr.2019.06.015.
Williams-Jones, A.E. and Vasyukova, O.V. (2023) Niobium, critical metal, and progeny of the mantle. Economic Geology and the Bulletin of the Society of Economic Geologists, 118, 837–855, https://doi.org/10.5382/econgeo.4994.
Williams-Jones, A.E., Samson, I.M., and Olivo, G.R. (2000) The genesis of hydrothermal fluorite-REE deposits in the Gallinas Mountains, New Mexico. Economic Geology and the Bulletin of the Society of Economic Geologists, 95, 327–341, https://doi.org/10.2113/gsecongeo.95.2.327.
Wu, H.H., Huang, H., Zhang, Z.C., Pan, B.B., Li, H.Z., Gao, Y.B., Gardiner, J.N., and Finch, A.A. (2024) Magmatic-hydrothermal evolution and rare metal enrichment of the Huoshibulake B-rich rare metal granite in the Southern Tianshan: insights from texture, geochemistry, and Hf-O isotopes of zircon. Lithos, 482-483,107705, https://doi.org/10.1016/j.lithos.2024.107705.
Xie, M.C., Xiao, W.J., Su, B.X., Sakyi, P.A., Ao, S.J., Zhang, J.E., Song, D.F., Zhang, Z.Y., Li, Z.Y., and Han, C.M. (2022) REE mineralization related to carbonatites and alkaline magmatism in the northern Tarim basin, NW China: Implications for a possible Permian large igneous province. International Journal of Earth Sciences, 111, 2759–2776, https://doi.org/10.1007/s00531-021-02138-1.
Yang, S.Y., Jiang, S.Y., Zhao, K.D., Dai, B.Z., and Yang, T. (2015) Tourmaline as a recorder of magmatic-hydrothermal evolution: An in situ major and trace element analysis of tourmaline from the Qitianling batholith, South China. Contributions to Mineralogy and Petrology, 170, 42, https://doi.org/10.1007/s00410-015-1195-7.
Yang, W.B., Niu, H.C., Li, N.B., Hollings, P., Zurevinski, S., and Xing, C.M. (2020) Enrichment of REE and HFSE during the magmatic-hydrothermal evolution of the Baerzhe alkaline granite, NE China: Implications for rare metal mineralization. Lithos, 358–359, 105411, https://doi.org/10.1016/j.lithos.2020.105411.
Zaraisky, G.P., Aksyuk, A.M., Devyatova, V.N., Udoratina, O.V., and Chevychelov, V.Y. (2009) The Zr/Hf ratio as a fractionation indicator of rare-metal granites. Petrology, 17, 25–45, https://doi.org/10.1134/S0869591109010020.
Zaraisky, G.P., Korzhinskaya, V., and Kotova, N. (2010) Experimental studies of Ta_2O_5 and columbite-tantalite solubility in fluoride solutions from 300 to 550 °C and 50 to 100 MPa. Mineralogy and Petrology, 99, 287–300, https://doi.org/10.1007/s00710-010-0112-z.
Zhang, R.X. and Yang, S.Y. (2016) A mathematical model for determining carbon coating thickness and its application in electron probe microanalysis. Microscopy and Microanalysis, 22, 1374–1380, https://doi.org/10.1017/S143192761601182X.
Zhang, C.L. and Zou, H.B. (2013) Permian A-type granites in Tarim and western part of Central Asian Orogenic Belt (CAOB): Genetically related to a common Permian mantle plume? Lithos, 172-173, 47–60, https://doi.org/10.1016/j.lithos.2013.04.001.
Zhang, C.L., Xu, Y.G., Li, Z.X., Wang, H.Y., and Ye, H.M. (2010) Diverse Permian magmatism in the Tarim Block, NW China genetically linked to the Permian Tarim mantle plume. Lithos, 119, 537–552, https://doi.org/10.1016/j.lithos.2010.08.007.
Zhao, H.D., Zhao, K.D., Palmer, M.R., and Jiang, S.Y. (2019) In-situ elemental and boron isotopic variations of tourmaline from the Sanfang granite, South China: Insights into magmatic-hydrothermal evolution. Chemical Geology, 504, 190–204, https://doi.org/10.1016/j.chemgeo.2018.11.013.
Zhao, H.D., Zhao, K.D., Palmer, M.R., Jiang, S.Y., and Chen, W. (2021a) Magmatic-hydrothermal mineralization processes at the Yidong Tin Deposit, South China: Insights from in situ chemical and boron isotope changes of tourmaline. Economic Geology and the Bulletin of the Society of Economic Geologists, 116, 1625–1647, https://doi.org/10.5382/econgeo.4868.
Zhao, Z., Yang, X.Y., Liu, Q.Y., Lu, Y.Y., Chen, S.S., Sun, C., Zhang, Z.Z., Wang, H., and Li, S. (2021b) In-situ boron isotopic and geochemical compositions of tourmaline from the Shangbao Nb-Ta bearing monzogranite, Nanling Range: Implication for magmatic-hydrothermal evolution of Nb and Ta. Lithos, 386–387, 106010, https://doi.org/10.1016/j.lithos.2021.106010.
Zhao, Z., Yang, X.Y., Lu, Y.Y., Zhang, Z.Z., Chen, S.S., Sun, C., Hou, Q., Wang, Y., and Li, S. (2022) Geochemistry and boron isotope compositions of tourmalines from the granite-greisen-quartz vein system in Dayishan pluton, Southern China: Implications for potential mineralization. American Mineralogist, 107, 495–508, https://doi.org/10.2138/am-2021-7591.
Zheng, B.Q., Chen, B., Sun, K.K., and Huang, C. (2022) Tourmaline as a recorder of the magmatic-hydrothermal evolution in the formation of pegmatite: In-situ elemental and boron isotopic compositions of tourmaline from the Qinghe pegmatite, Chinese Altay orogen. Journal of Asian Earth Sciences, 231, 105224, https://doi.org/10.1016/j.jseaes.2022.105224.
Zhu, Z.Y., Wang, R.C., Che, X.D., Zhu, J.C., Wei, X.L., and Huang, X.E. (2015) Magmatic-hydrothermal rare-element mineralization in the Songshugang granite (northeastern Jiangxi, China): Insights from an electron-microprobe study of Nb-Ta-Zr minerals. Ore Geology Reviews, 65, 749–760, https://doi.org/10.1016/j.oregeorev.2014.07.021.
Zong, Z.J., Du, Y.S., Li, S.T., Cao, Y., Du, J.G., Deng, X.H., and Xue, L.W. (2020) Petrogenesis of the early Permian A-type granites in the Halajun region, southwest Tianshan, western Xinjiang, NW China: Implications for geodynamics of Tarim large igneous province. International Geology Review, 63, 1110–1131, https://doi.org/10.1080/00206814.2020.1749898.

Manuscript received July 20, 2023
Manuscript accepted January 5, 2024
Accepted manuscript online January 18, 2024
Manuscript handled by Paul Tomascak

Endnote:

[1]Deposit item AM-24-89131. Online Materials are free to all readers. Go online, via the table of contents or article view, and find the tab or link for supplemental materials.